UNIVERSITÀ DEGLI STUDI DI TRIESTE

XXXII CICLO DEL DOTTORATO DI RICERCA IN

Scienze della Terra e Meccanica dei Fluidi

Levantine intermediate and deep water formation and water mass characteristics: An Argo float study from 2000 to 2017

Settore scientifico-disciplinare: **GEO/12**
OCEANOGRAFIA E FISICA DELL'ATMOSFERA

DOTTORANDO / A
ELISABETH KUBIN

COORDINATORE
PROF. PIERPAOLO OMARI

SUPERVISORE DI TESI
PROF. PIERRE-MARIE POULAIN

CO-SUPERVISORE DI TESI
M.Sc. ELENA MAURI

ANNO ACCADEMICO 2018/2019

Levantine intermediate and deep water formation and water mass characteristics: An Argo float study from 2000 to 2017

Elisabeth Kubin

University of Trieste

A thesis submitted for the degree of

Doctor of Philosophy

March 2020

This thesis is dedicated to
my grandmother *Marianne Kubin*
who taught me the value of nature,
the interconnectedness of life and
who was the best storyteller ever.

'Everything depends upon the give-and-take between ourselves and our work; upon the product which we contribute to the [...] world, and upon that constant feed-back that can be amplified by conscious self-criticism. The incredible thing about life, evolution, and mental growth, is just this method of give-and-take, this interaction between our actions and their results by which we constantly transcend ourselves, our talents, our gifts. This self-transcendence is the most striking and important fact of all life and all evolution, and especially of human evolution.'

[Karl Popper]

Acknowledgements

The ocean is a living being, an oscillating vibrating system. The ocean is life and therefore a mystery and cannot be fully understood. Breathe the ocean spray, listen to the breaking waves, touch the sacred, life-giving waters that cry out for protection, awareness, thankfulness. Listen in silence and receive; nature gives us so much and all we have to do is to listen to her, entering without harming. Mitakuye Oyasin.

First of all, I would like to thank my parents for their care and love they were (and are) giving to my son Tomás. Without their support this thesis would hardly have been possible.
Second, I want to thank all women, especially mothers, who have been and are still fighting for a better world; due to their efforts, I now have the right to vote, to study and to lead an independent life.
Furthermore, I would like to thank Pierre-Marie Poulain for giving me the opportunity to work with Argo floats, in such an interesting field as oceanography. Thanks also go to Milena Menna, for scientific advices and for her constant support throughout these years, becoming a dear friend. Thanks also to all my friends for dedicating time, dinners and music together.
Last, but not least, I would like to thank Tomás for his creativity, joy and kindheartedness.

Abstract

Levantine intermediate water (LIW) is formed in the Levantine Sea (Eastern Mediterranean) and spreads throughout the Mediterranean at intermediate depths, following the general circulation. The LIW, characterized by high salinity and relatively high temperatures, is one of the main contributors of the Mediterranean Overturning Circulation and influences the mechanisms of deep water formation in the Western and Eastern Mediterranean sub-basins. LIW also affects the ecological system (e.g. the depth of the nutricline) and the Mediterranean Outflow into the Atlantic Ocean, hence in some extent, world climate.
In this study, the LIW and Levantine deep water (LDW) formation processes are investigated using Argo float data from 2001 to 2017 in the Northwestern Levantine Sea (NWLS), the larger area around Rhodes Gyre (RG). To find pronounced events of LIW and LDW formation, more than 800 Argo profiles were analyzed visually. Events of LIW and LDW formation captured by the Argo float data were compared to buoyancy, heat and freshwater fluxes, sea surface height (SSH), and sea surface temperature (SST). All pronounced events (with a mixed layer depth (MLD) deeper than 250 m) of dense water formation were characterized by low surface temperatures and strongly negative SSH. The formation of intermediate water with typical LIW characteristics (potential temperature>15 ℃, salinity>39 psu) occurred mainly along the Northern coastline, while LDW formation (13.7 ℃<potential temperature<14.5 ℃, 38.8 psu<salinity<38.9 psu) occurred during strong convection events within temporary and strongly depressed mesoscale eddies in the center of RG. This study reveals and confirms the important contribution of boundary currents in ventilating the interior ocean and therefore underlines the need to rethink the drivers and contributors of the thermohaline circulation of the Mediterranean Sea.

Contents

List of Figures

List of Tables

Chapter 1

Introduction

The Mediterranean Sea (Figure 1.1) is composed of two basins of nearly equal size, the Western and the Eastern Mediterranean Sea, connected by the Sicily Channel. The general circulation of the Mediterranean Sea can be divided into three dominant scales of motion: the basin scale including the thermohaline circulation, the sub-basin scale including permanent and quasipermanent cyclonic and anticyclonic gyres, and the mesoscale with small but energetic temporary eddies ([3,10], Figure 1.2). All these scales are interacting.

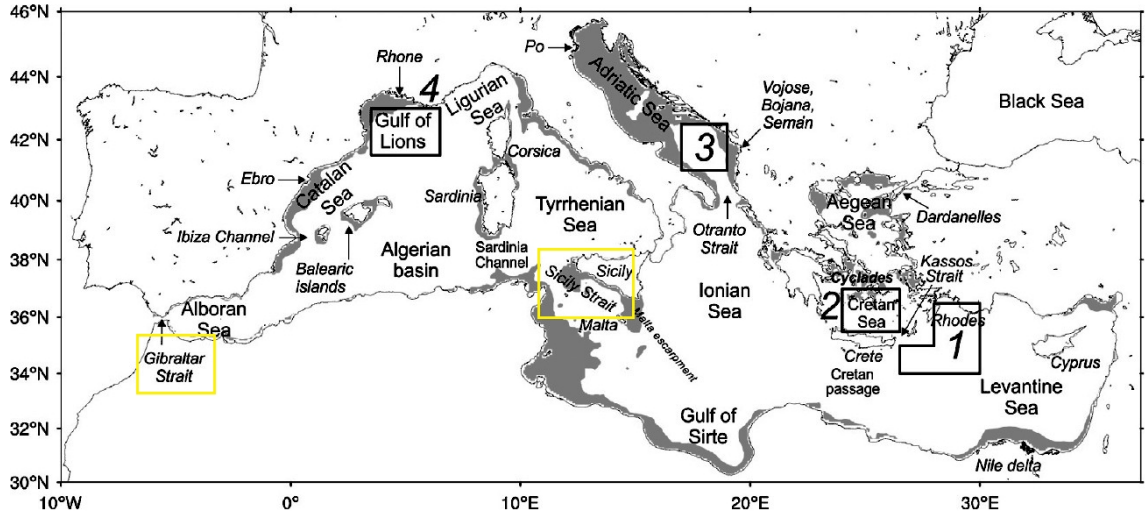

Figure 1.1: The Mediterranean Sea and its mayor sub-basins and straits. Shaded areas indicate depths less than 200 m. Boxes 1-4 (Rhodes Gyre, Cretan/Aegean Sea, South Adriatic, Gulf of Lions) show the Mediterranean deep dense water formation sites which in the prevailing view are driving the thermohaline circulation of the Mediterranean Sea. Adapted from [1].

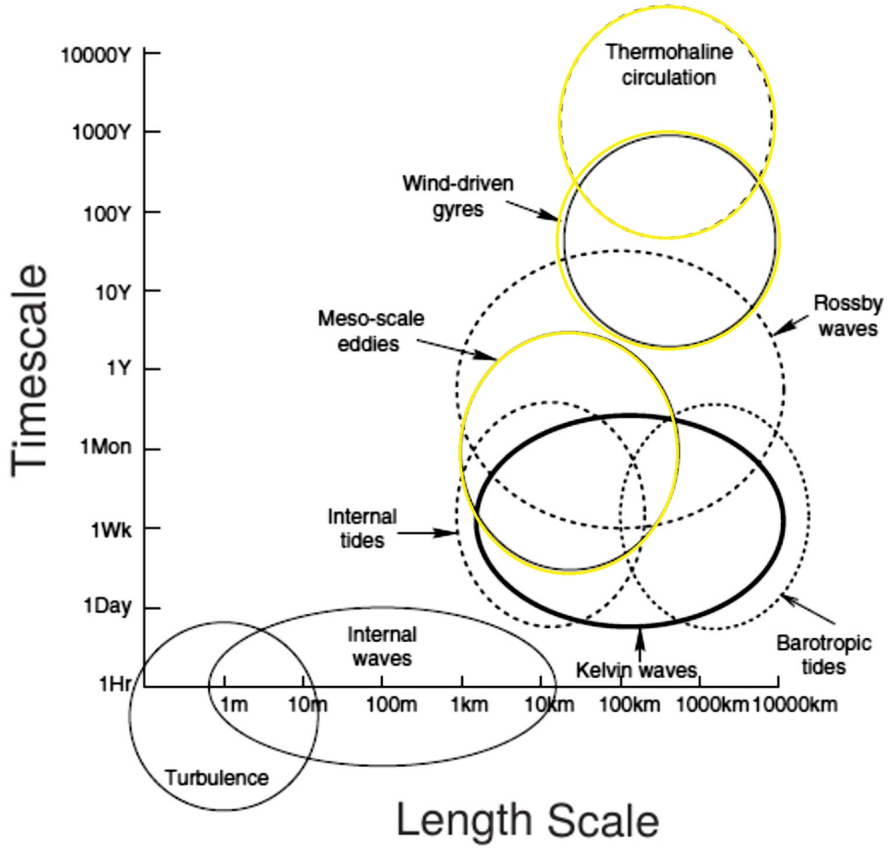

Figure 1.2: Length and time scales of oceanographic features. Adapted from [2].

Through the Strait of Gibraltar, the relatively fresh Atlantic water (AW) enters the Western Mediterranean Sea within the upper 100 to 200 m (Figure 1.3). It is modified flowing eastward, passes the Sicily Channel and the Ionian Sea and enters the easternmost part of the Mediterranean, the Levantine Sea. The salinity of the AW in the Levantine Sea depends on the circulation patterns during its path, mainly influenced by the variability of the circulation of the North Ionian Gyre (NIG) which varies significantly at seasonal and decadal scales ([11–13], Figure 1.4a).

Due to evaporation and air-sea exchanges, the AW is becoming saltier and warmer when reaching the Levantine Sea. The AW that enters the Levantine Sea is identified by a subsurface minimum of S<38.6 psu and by a temperature of 14-15 ℃. The Levantine intermediate waters (LIW) properties are defined by salinity values greater than 39 psu, potential temperature values greater than 15 ℃ and potential density values between 29 and 29.05 kgm^{-3}, while typical ranges for Levantine deep water (LDW) are 13.7-14.5 ℃ and 38.8-38.9 psu [9].

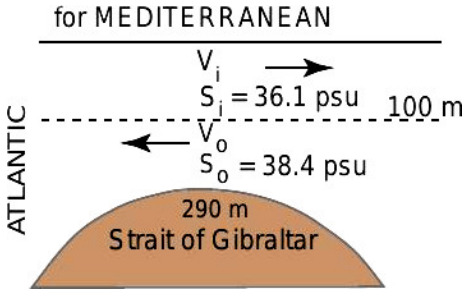

Figure 1.3: Water mass exchanges at the Strait of Gibraltar.

The strong advective surface salinity preconditioning [14] and buoyancy losses due to heat and freshwater fluxes in winter lead to dense water formation, sinking takes place, and the LIW is formed (Figure 1.4a). The LIW is characterized by a subsurface salinity maximum and occupies and moves in the intermediate layers between 200 and 600 m throughout the Mediterranean Sea until it reaches the Atlantic Ocean through the Strait of Gibraltar. Therefore, the LIW contributes as an important driver to the thermohaline circulation of the Mediterranean Sea. The specific pathways of the thermohaline circulation depend strongly on where and when the LIW is formed.
According to the prevailing view, the LIW formation takes place within the cyclonic Rhodes Gyre (RG) during the winter months ([3, 15], Figure 1.4a). However, experimental studies showed that the RG is also a place of LDW formation and that the Levantine basin is a site of multiple and different water mass formation processes [9, 16, 17]. Furthermore, recent theoretical models revealed that no net mean sinking takes place within Mediterranean convection sites such as the RG, while boundary currents undergo net intense sinking ([5, 18–22]; mean from 1980 to 2013 for all seasons; Figure 1.4c). This is due to vorticity dynamics: Only dissipation at the boundary (and bottom friction) can balance the vortex stretching that arises from vertical motions induced by net sinking (see Chapter 2:Theory).
The pathway of sinking water masses depends also on the bathymetry (Figure 1.5), following isopycnals or/and the continental shelf slope and filling the basins of the Levantine Sea with dense and cold waters, called Eastern Mediterranean Deep Water (EMDW).
The focus of the study is on the Northwestern Levantine Sea (NWLS; latitude: 33 °-37 °, longitude: 26 °-32 °; yellow rectangle in Figure 1.4b), the larger area around the RG, including also the area along the Northern coast.
The NWLS is characterized by a general cyclonic surface circulation and the presence of the permanent RG, cyclonic and anticyclonic structures (such as Ierapetra (IG) and Mersa-Matruh Eddy (MME)), intense jets (such as the Mid Mediterranean Jet (MMJ); with minimum subsurface salinity values), a strong coastal current along the Northern coastline (the Asia Minor Current (AMC)), and the passage from the Cretan to the Levantine Sea ([4], Figure 1.4b).

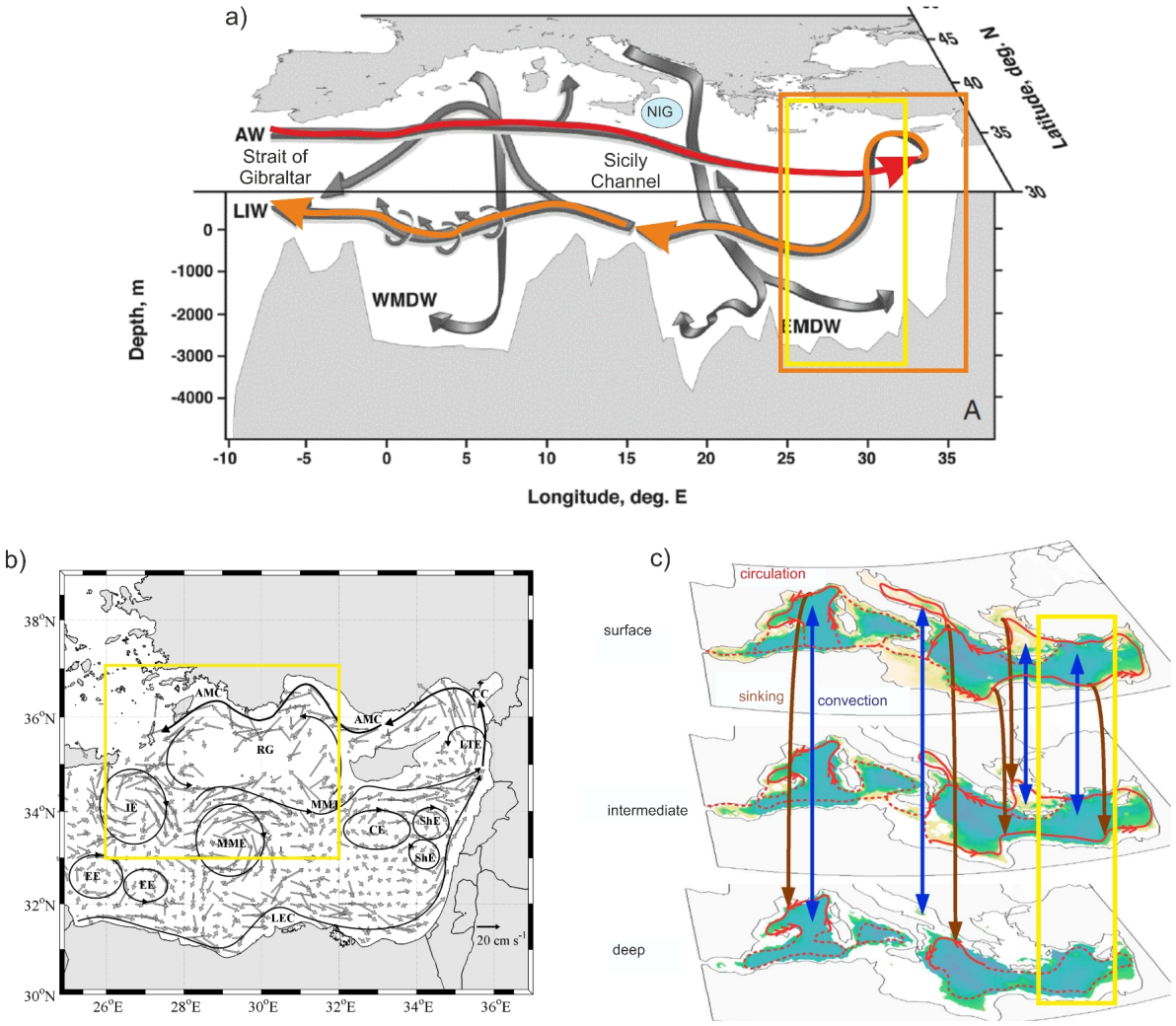

Figure 1.4: a) General concept of the thermohaline circulation which, according to the prevailing view, is driven by a few convection sites within the Mediterranean Sea, adapted from [3]. The red arrow shows the entering Atlantic water (AW) while the orange arrow shows the Levantine intermediate water (LIW), which travels throughout the Mediterranean and flows into the Atlantic Ocean. The orange and yellow frames highlight the area of the Levantine Sea and of the Northwestern Levantine Sea (NWLS), respectively. The blue circle indicates the position of the North Ionian Gyre (NIG) the circulation of which is important for the advective salinity preconditioning. b) Mean surface geostrophic circulation in the Levantine Sea from 1992 to 2010 derived from drifter data. The yellow rectangle indicates the area of study, the NWLS (latitude: 33-37°, longitude: 26-32°). Adapted from [4]. AMC-Asia Minor Current; CC-Cilician Current; CE-Cyprus Eddy; EE-Egyptian Eddies; IE-Ierapetra Eddy; LEC-Libyo-Egyptian Current; LTE-Latakia Eddy; MME-Mersa-Matruh Eddy; MMJ-Mid Mediterranean Jet; ShE-Shikmona Eddy. c) A model run from 1980 to 2013 [5] showed that little to no net sinking takes place at convection sites (blue arrows; from left to right: Gulf of Lion, South Adriatic, Aegean Sea, Rhodes Gyre (RG)) while boundary layer currents undergo net intense sinking (brown arrows). The yellow rectangle indicates the area of study. Adapted from [5].

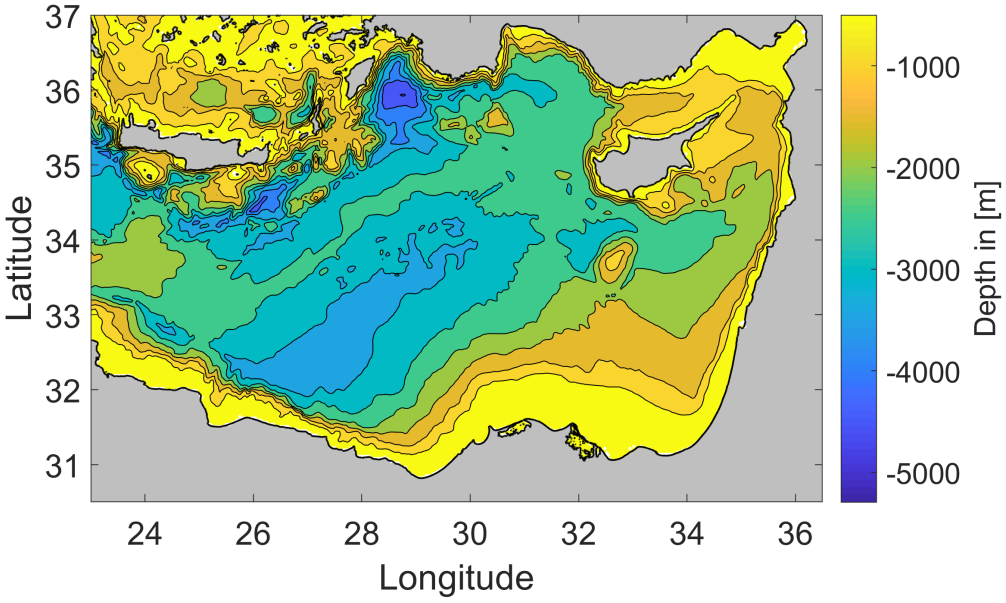

Figure 1.5: Bathymetry of the Levantine Sea in 500 m steps

The study aims to describe where and when LIW and LDW formation take place within the NWLS, using Lagrangian Argo float data over a period of 16 years, i.e. from the first deployments of Argo float data in the specified area. The results were compared to heat and freshwater fluxes and satellite data (SSH, SST).
Dense water formation processes occur on daily scales and are linked to temperature and salinity extrema which are not represented using climatological data sets or mixed layer depth (MLD) detection algorithms. Therefore, more than 800 Argo float profiles from 2001 to 2017 were analyzed visually to investigate LIW and LDW formation during winter months.

The thesis is divided into chapters and sections: In Chapter 2, the theory, and in Chapter 3, data sets and analysis methods are presented. In Section 4.1, the Argo float statistics of float speed, residence time, MLD and ocean heat content are shown. In Section 4.2.1, the time evolution of heat, freshwater and buoyancy fluxes from 2001 to 2017 for the center of the RG are shown to identify periods of extreme heat losses due to outbreaks of strong cold and dry winds leading to dense water formation. Section 4.2.2.1 gives two examples of LDW formation within the RG and one example of typical LIW formation along the Northern coastline and characterizes the newly formed water masses. In Section 4.2.2.4, intermediate water mass characteristics are shown for different areas within the entire Levantine Sea. Chapter 5 gives an overall discussion and summarizes the major results.

Chapter 2

Theory

The ocean is a complex and turbulent system, therefore it is astonishing that pronounced circulation patterns such as the Gulf Stream, large gyres, mesoscale eddies and upwelling at the equator or along eastern coastlines, can be explained by basic physical forces such as the pressure gradient forces, frictional forces and the Coriolis force.
Conservation laws lead to the basic equations of fluid motion: The conservation of mass leads to the continuity equation, the conservation of energy leads to the heat budgets, the conservation of mechanical energy leads to the wave equation, the conservation of momentum leads to the (momentum) Navier-Stokes equation and the conservation of angular momentum leads to the conservation of vorticity [2, 6, 23–25].

This chapter will describe two theoretical concepts used in the thesis: the geostrophic approximation, derived from the Navier-Stokes equation, for the calculation of Sea Surface Height (SSH) by satellite altimetry and the conservation of potential vorticity for describing the sinking of water masses along boundary currents.

2.1 Navier-Stokes equation

The Navier-Stokes equation describes the Lagrangian movement of an individual particle. The Lagrangian description of motion follows a fluid element, therefore the Lagrangian (material) derivative is the local rate of change at a given point plus the advective derivative.

$$\underbrace{\frac{\delta u}{\delta t} + (u\nabla)u}_{1} = \underbrace{-\frac{1}{\rho}\nabla p}_{2} + \underbrace{\nu\nabla^2 u}_{3} + \underbrace{g}_{4} + \underbrace{2(\Omega \times u)}_{5}$$

1. Lagrangian derivative composed of the local rate of change and the advective derivative; $u = (u, v, w)$ is the velocity vector.

2. Gradient pressure force; ρ is the seawater density and ∇p the pressure gradient

3. Frictional force; ν is the kinematic viscosity

4. Gravity force; g is the vector of gravity acceleration

5. Coriolis force; Ω is the angular velocity vector of the Earth rotation

A scale analysis discusses the orders of magnitude and estimates the relative sizes of the different terms. A scale for every variable is introduced, with a representative numerical value (e.g. time, velocity, length scale). The scale values vary with every application.
Dimensionless numbers such as the Rossby Ro, the temporal Rossby Ro_T, the Ekman Ek and the Richardson Ri numbers, indicate the ratio of forces [25].

2.2 Geostrophic Approximation

If we assume a homogenous fluid ($\rho = const.$), ignore frictional effects and assume that the Coriolis acceleration dominates the various acceleration terms, the geostrophic approximation can be made ($Ro \ll 1$, $Ro_T \ll 1$, $Ek \ll 1$), i.e. the horizontal pressure gradient force balances the Coriolis force:

$$-f \cdot v = \frac{1}{\rho} \cdot \frac{\delta p}{\delta x}$$

$$+f \cdot u = \frac{1}{\rho} \cdot \frac{\delta p}{\delta y}$$

$$0 = -\frac{1}{\rho} \cdot \frac{\delta p}{\delta z}$$

where $f = 2\omega sin\varphi$ is the Coriolis parameter with latitude φ.

The continuity equation, that derives from the conservation of mass, with the Boussinesq approximation ($\rho' \ll \rho$) can be written as:

$$\frac{\delta u}{\delta x} + \frac{\delta v}{\delta y} + \frac{\delta w}{\delta z} = 0$$

The vertical derivative of the horizontal velocity is zero. This result is known as the Taylor-Proudman-Theorem and means that the horizontal velocity field has no vertical shear and all particles move in concert, indicating the typical vertical rigidity of rotating homogenous fluids.

The velocity vector (u, v) is perpendicular to the pressure gradient vector, therefore the flow is not down-gradient, but across-gradient. All fluid-elements flow along lines of constant pressure (isobars) with the geostrophic velocity (u, v):

$$u = \frac{-1}{\rho f} \cdot \frac{\delta p}{\delta x} \quad , \quad v = \frac{+1}{\rho f} \cdot \frac{\delta p}{\delta y}$$

The geostrophic velocity depends on the latitude φ and on the horizontal pressure gradient ∇p and increases with growing pressure gradient. At the equator the horizontal component of the Coriolis force is zero and the equation is not applicable.

The current speed is proportional to the slope of the horizontal pressure gradient force, i.e. to the slope of the sea surface. The flow is barotropic, i.e. that lines of constant p and ρ are parallel. The resulting currents flow along the contour lines of sea surface height (SSH; barotropic flow), so that sea level is high on the right (left) of the flow direction in the Northern (Southern) hemisphere (Figure 2.1). The SSH anomaly allows the calculation of the geostrophic currents at the surface by satellite altimeters (as used in this study) [26].

In reality, due to frictional forces and density differences, the flow is baroclinic and lines of constant p and ρ are not parallel. Therefore upwelling (downwelling) occurs within cyclonic (anticyclonic) gyres and eddies, leading to anticylonic warm-core and cyclonic cold-core eddies (for the Northern hemisphere; Figure 2.2).

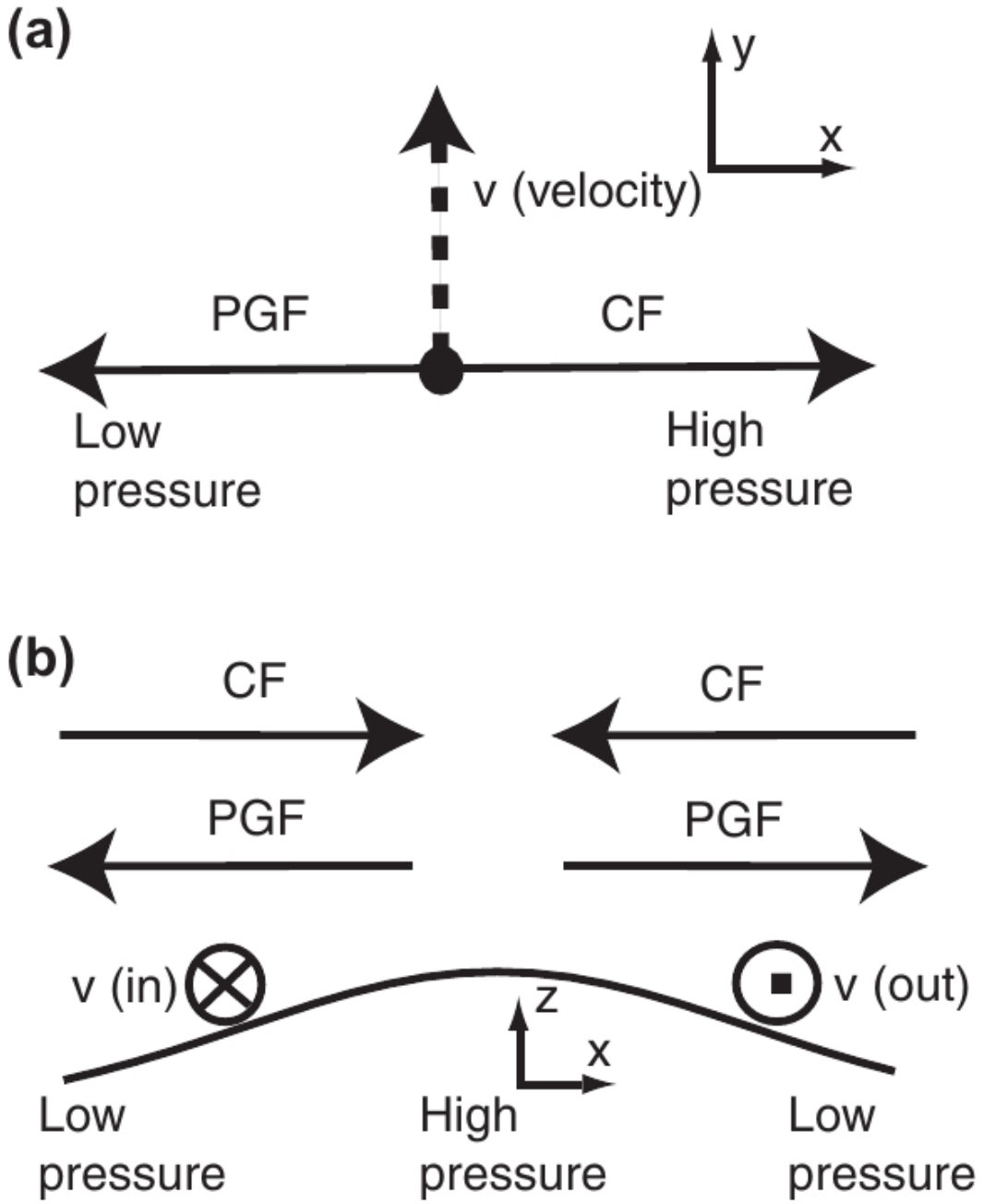

Figure 2.1: Description of the geostrophic balance for the Northern hemisphere (PFG-Pressure gradient force; CF-Coriolis force). a) Looking down onto the ocean. b) Looking at a cross-section [6].

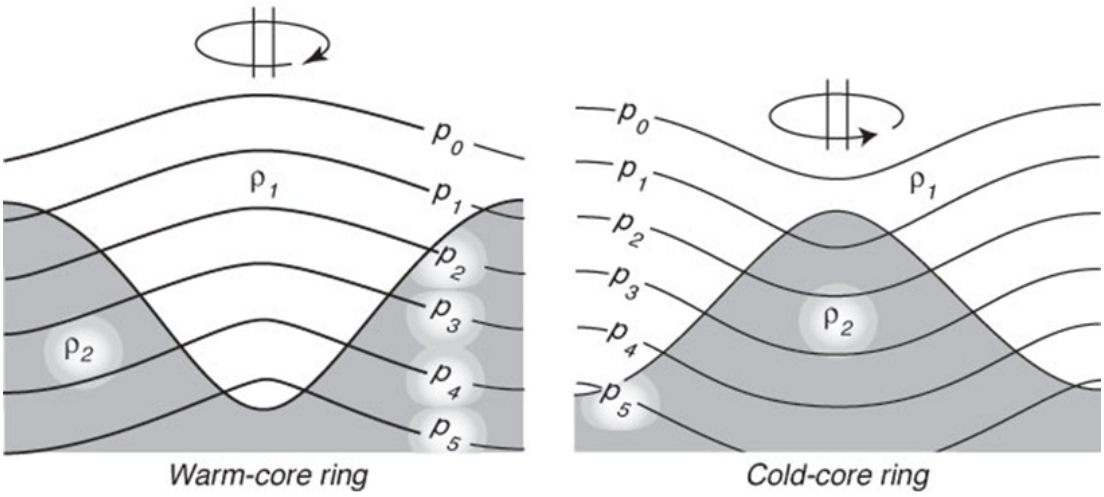

Figure 2.2: Constant pressure surfaces p_0 and the interface between two water masses of density ρ_1 and ρ_2 for the Northern hemisphere. Left: Anticyclonic motion, warm-core eddy. The sea surface p_0 slopes up toward the center of the warm-core ring, while the constant-density surfaces slope down toward the center. Right: Cyclonic, cold-core eddy. The sea surface p_0 slopes down toward the center of the cold-core ring, while the constant-density surfaces slope up toward the center [6].

2.3 Potential Vorticity

The conservation of angular momentum leads to the conservation of vorticity. The potential vorticity q couples changes in depth H (due to water column stretching or squeezing), changes in relative vorticity ζ (due to fluid circulation) and changes in the Coriolis parameter f (changes with latitude due to the earth rotation).

$$q = \frac{f + \zeta}{H}$$

The potential vorticity q has to be conserved.

- To conserve potential vorticity for a barotropic flow over a sea mountain (squeezing of the water column H), the flow has to turn equatorward. This is called topographic steering.
- If a column of water ($H = const.$) moves equatorward, the planetary vorticity f decreases and therefore the relative vorticity ζ must increase.
- If the planetary vorticity $f = const$, i.e. if the latitude is constant, and vortex stretching ($\Delta H > 0$) is induced by sinking water masses, then the relative

vorticity ζ has to increase: This is only possible with lateral or bottom friction. Therefore only lateral (shear stress of boundary currents) or bottom friction can balance the vortex stretching induced by sinking.

This theoretical fact is important for the explanation of the final results of this study.

Chapter 3

Datasets and Methods

3.1 Datasets and Methods

3.1.1 Argo floats

Argo floats (Figure 3.1) are autonomous Lagrangian instruments that float with the ocean currents.

With the help of an external bladder, the Lagrangian floats descend to a programmed parking depth (350 or 1000 m) where they stay for a specified period (1-10 days, mainly 5 days; Figure 3.2, [27]). Then, they descend to greater depths (up to 2000 m).
During their ascent back to the surface, they measure temperature and salinity throughout the water column. Bio-Argo floats additionally measure biogeochemical parameters such as oxygen, nutrients, pH and chlorophyll-a. At the surface they transmit the data to satellites and descend again. The transmitted data are stored at data assembly centers (DAC) which apply a quality control and provide open access to real time and delayed mode quality controlled data.

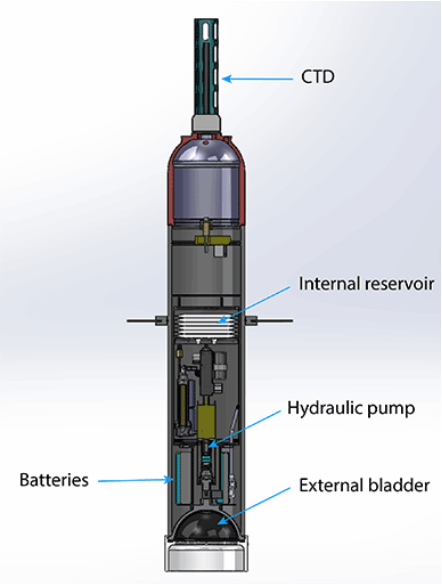

Figure 3.1: Schematic of an Argo float [7].

Quality controlled Argo float data (netcdf files) were downloaded from the Ifremer Data Assembly Center (DAC; ftp://ftp.ifremer.fr/ifremer/argo/dac/coriolis/). For this study, only delayed mode data with the best quality control (qc=1) were taken into account. Downloaded parameters included float number, position, time, pressure, temperature, and salinity.

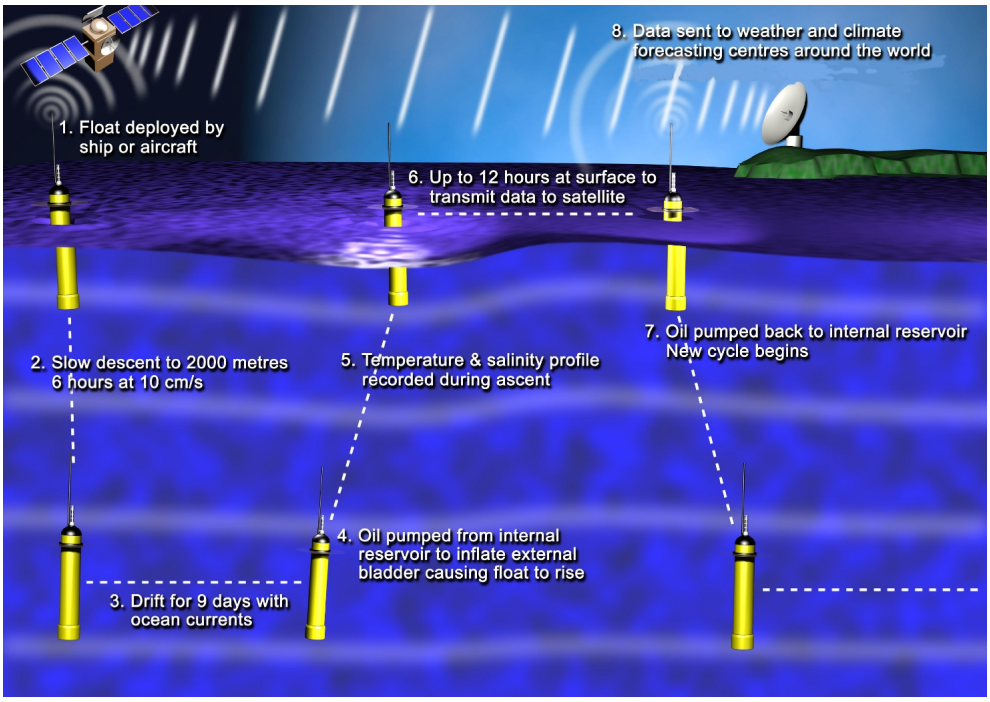

Figure 3.2: Argo cycles [7].

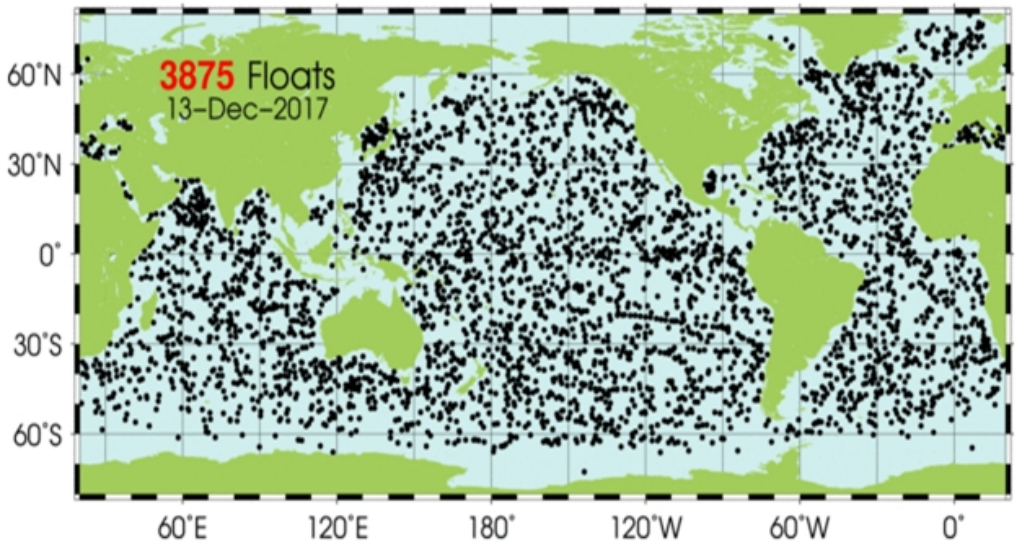

Figure 3.3: Global Argo array in 2017 [7].

ARGO is a global array of 3.800 (2017) free-drifting profiling floats (Figure 3.3). The Argo data are collected and made freely available by the International Argo Program and the national programs that contribute to it (http://www.argo.ucsd.edu, http://argo.jcommops.org). The Argo Program is part of the Global Ocean Observing System.

3.1.2 Argo float data set for the Levantine Sea

The annual float profile distribution within the Levantine Sea and the corresponding data points and float trajectories from 2000 to 2017 are shown in Figure 3.4. The total number of Argo floats within the specified area and time period were 50, the total number of Argo float profiles were 8079 and the maximum residence time of one single float was about 6 years, while the mean residence time was about 2 years. The residence time of all floats during this period equals to about 100 years.

Total number of floats:	50
Residence time of all floats:	102.7 years
Max residence time of one single float:	5.8 years
Mean residence time:	2.1 years
Total number of profiles:	8079

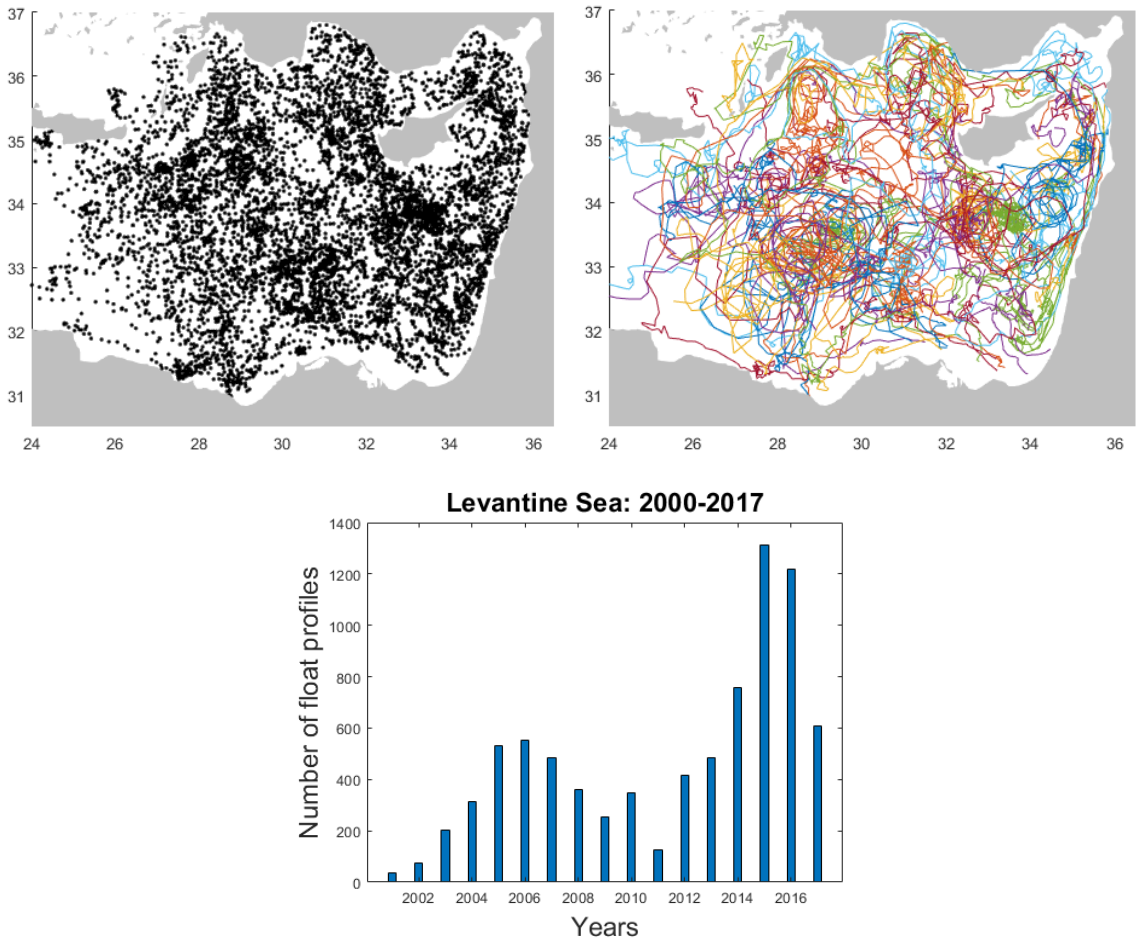

Figure 3.4: Upper panel: Float profiles and float trajectories within the Levantine Sea from 2000 to 2017. Lower Panel: Annual float profile distribution within the area of the Levantine Sea from 2000 to 2017.

3.1.3 Statistics of float speed and residence time

The speed and residence time of different water masses give a better understanding of the general circulation. Therefore the mean float speed and mean float residence times have been calculated for two different parking depths: PD=350 m (intermediate layers) and PD=1000 m (deeper waters). Only delayed mode data with the best quality control (qc=1) were used. Float speed and float residence time were calculated for $1° \times 1°$ bins within the Levantine Sea from 2000 to 2017, using only float data with 5 day cycles. To calculate the speed and residence time, the parameters of float position and time were used. The surfacing time of the floats (for sending the data to the satellites) was not considered.

3.1.4 Statistics of mixed layer depth and ocean heat content

The $1° \times 1°$ bin MLD climatologies, derived from Argo float data and calculated by a hybrid algorithm that models the shape of each pofile, searching for physical features to find the most suitable MLD, were downloaded from [28]. Mean, maximum and winter maximum MLD climatologies were plotted from 2000 to 2018 for the area of the Levantine Sea.
For the $1° \times 1°$ bin climatology of the ocean heat content (OHC), different formulas were found in literature:

1. $HC = \int \rho(z) * c_p * T(z) * dz$ (Bensi, Rubino)

2. $HC = \int \rho(z) * c_p(\theta, S) * \theta(z) * dz$ (Artale)

3. $HC = \int \rho(z) * c_p * \theta(z) * dz$ (paper Vedrana and Jorda et al., 2017)

4. $HC = \int \rho_{\theta(z)} * c_p(\theta, S, z) * \theta(z) * dz$

where ρ is the density, c_p is the specific heat capacity of seawater, T is the temperature, θ is the potential temperature and $\rho_{\theta(z)}$ is the potential density.

Formulas 1-4 were plotted and compared to each other (e.g. Figure 3.5 where Formula (1) was compared to Formula (4)). The results were not influenced significantly by using a constant specific heat capacity, temperature and density instead of potential temperature, potential density and variable heat capacity and therefore the mean heat content of the water column (until a maximum of about 2000 m) was calculated as:

$$meanHC = mean(c_p * \theta(z) * \rho_{\theta(z)}) \tag{3.1}$$

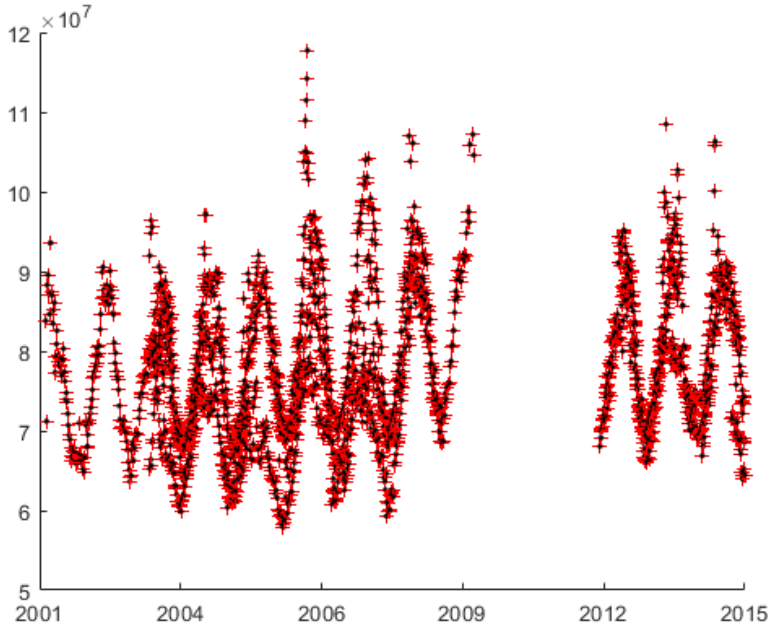

Figure 3.5: HC-Formula (1) compared to HC-Formula (4) for the upper 100 m from 2001 to 2015 within the Levantine Sea.

below different depths ($< 0m$, $< 50m$, $< 100m$, $< 500m$).

3.1.5 Argo float data set for the Northwestern Levantine Sea

The datasets used for this study are Argo floats vertical profiles of temperature and salinity (T/S) collected in the NWLS during winter months (January, February, March-JFM) between 2001 and 2017. In total 879 T/S profiles from 20 floats were analyzed visually (i.e. the *shapes* of the profiles were analyzed). Figure 3.6 shows the position of the Argo float profiles and the annual distribution of profiles for JFM between 2001 and 2017 for the area of study.

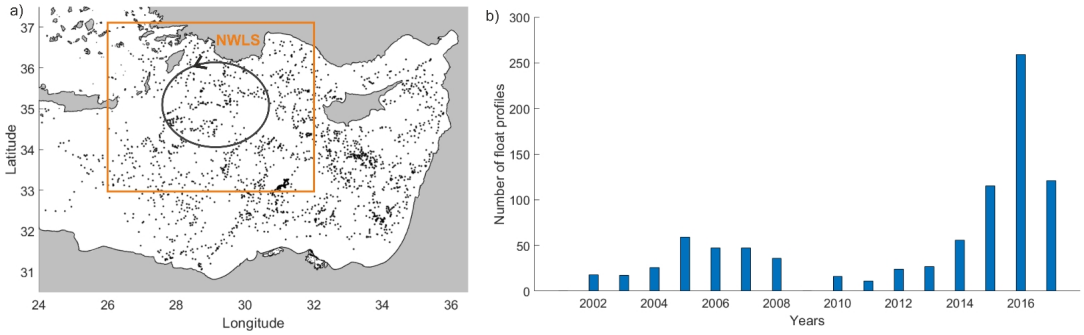

Figure 3.6: Left: Position of the 879 analyzed float profiles for January, February, and March (JFM) 2001-2017; the orange rectangle defines the area of study (the NWLS), the black ellipse describes the center of RG. Right: Annual distribution of float profiles in the NWLS: JFM 2001-2017.

Hydrographic properties were expressed as potential temperature, potential density, and salinity according to the practical salinity scale (PSU).
The visual inspection of the Argo float profiles is important due to the fact that the Argo floats may pass an area not exactly during the event of mixing or convection. They can instead sample days or weeks later when the recapping (i.e., a newly formed shallow MLD) already occurred. In such a case, MLD detection algorithms indicate a shallow MLD, but do not give any information about mixing or convection events before the recapping. While at the top, there can be already a newly formed MLD and the convection event can still be visible deeper in the water column. MLD detection statistics rarely give information about deep mixing events while the visual inspection of the form of the profile (potential temperature, salinity, and potential density) reveals clearly such events. Figure 3.7a shows the climatology of the winter maximum MLD derived from Argo float data and downloaded from [28] in the period 2000 to 2018. The maximum MLD is 225 m along the coastline of the NWLS (Figure 3.7a). The visual inspection of the Argo profiles in the same region reveals deeper dense water formation events. For example, in winter 2007, the float WMO 6900098 (Figure 3.7b), moving along the northern coastline of the NWLS, shows the deepening of the winter MLD from 100 m (Figure 3.7c) to 200 m (Figure 3.7d) in January. In March, when the maximum MLD is about 550 m, the recapping occurred (due to surface warming) with a newly formed MLD of about 50 m (Figure 3.7e). In this case, the MLD detention algorithm can fail, indicating the depth of 50 m as maximum MLD.

3.1.6 Satellite data

The SST and sea surface height (SSH; see also Chapter 2:Theory)) data were downloaded from Copernicus (marine.copernicus.eu). The interpolated SST product [1] has

[1] SST_MED_SST_4_NRT_OBSERVATIONS_010_004_c_V2

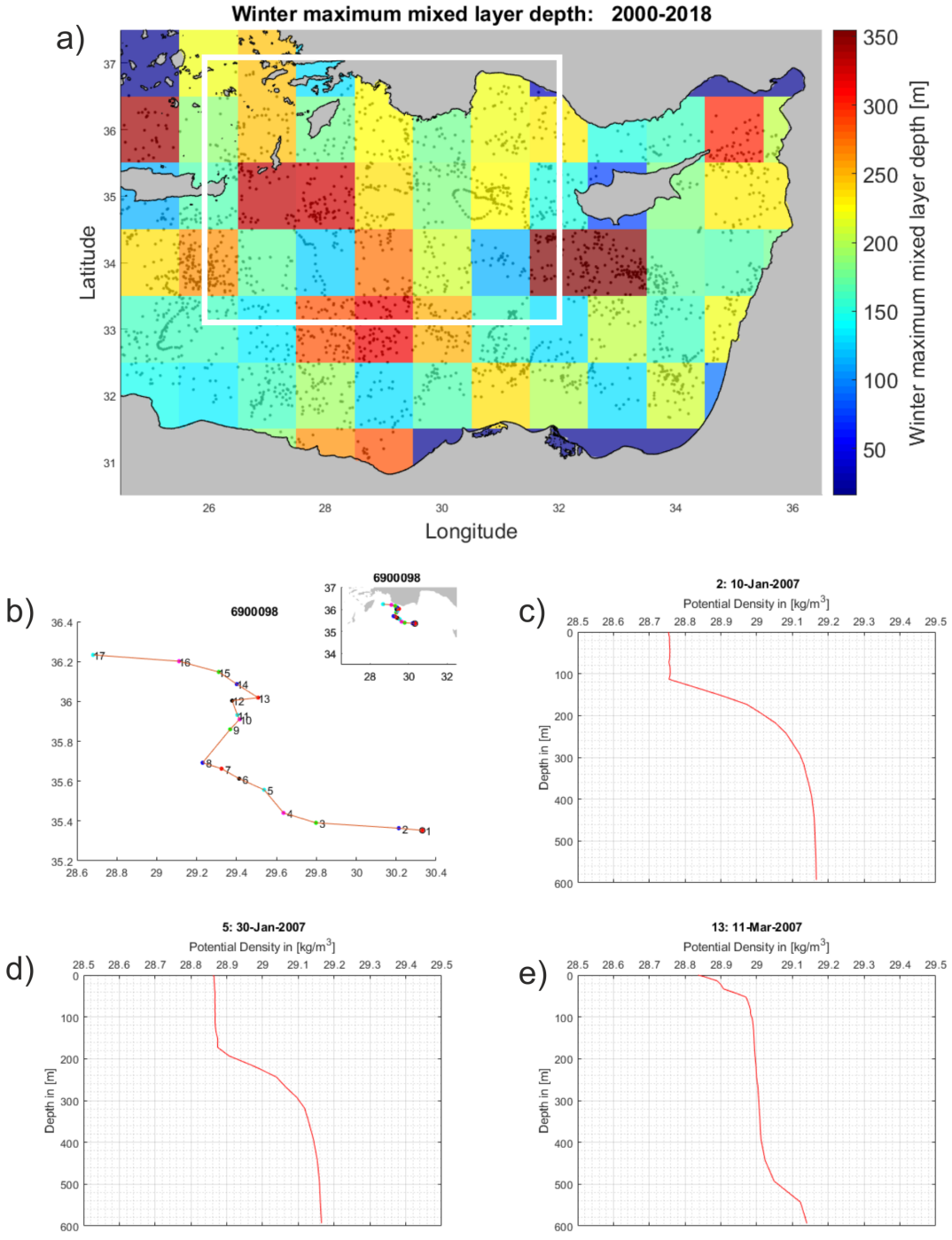

Figure 3.7: a) Climatology of the winter maximum mixed layer depth (colors) and location of float profiles (grey dots) from 2000 to 2018. The white rectangle indicates the area of study, the NWLS. b) Trajectory of the float WMO 6900098 during JFM 2007; the numbers along the trajectory show the locations of float profiles. Float potential density profiles at cycle 2 (c), 5 (d), and 13 (e).

a daily temporal resolution and a spatial resolution of 0.04° × 0.04°. The interpolated SSH product [1] has a daily temporal resolution and a spatial resolution of 0.125° × 0.125°. Monthly means of SST superimposed with the geostrophic currents from SSH were used to describe the negative slope of eddies within the RG during intense convection events.

3.1.7 Buoyancy fluxes

The surface buoyancy flux B, composed by thermal (B_T) and haline (B_S) components, was calculated according to [20]:

$$B = \alpha * g * (C_p{*}\rho 0)^{-1} * Qnet - \beta * S0 * g * (\rho 0)^{-1} * (E - P)$$

where α is the thermal expansion coefficient, $g = 9.8ms^{-2}$ is the gravity acceleration, $C_p = 3.9715 * 10^{-3}Jkg^{-1}K^{-1}$ is the specific heat capacity of sea water, $\rho 0 = 1029kgm^{-3}$ is a reference sea water density, β is the haline contraction coefficient and $S0 = 38.9$ is a reference salinity. α and β were calculated at surface pressure, using monthly mean surface salinity and monthly mean surface temperature, downloaded from Copernicus (MEDSEA_REANALYSIS_PHYS_006_004).

The freshwater fluxes (E-P) were derived from ERA-INTERIM (daily) data. The downloaded parameters are evaporation (E) and total precipitation (P). The downloaded data have a time step of 12 hours, i.e., daily data at 00:00:00 and at 12:00:00 and a spatial resolution of 0.25° × 0.25°. The daily freshwater fluxes (FWF) were calculated as the subtraction of the daily means of E and P: FWF = E - P.
The air-sea heat fluxes were derived from ERA-INTERIM (daily) data. The downloaded parameters are: Surface net solar radiation (Q_{sw}), surface net thermal radiation (Q_{lw}), surface sensible heat flux (Q_s), and surface latent heat flux (Q_l). The heat budget can be expressed as the difference between the net shortwave solar radiation (incoming minus reflected) absorbed by the sea surface, the sum of the longwave back radiation, the sensible, the latent, and the advective heat flux. The advective heat flux (Q_{adv}) was not available at ERA-INTERIM and therefore not considered. The downloaded data have a time step of 12 hours, i.e., daily data at 00:00:00 and at 12:00:00 and a spatial resolution of 0.25° × 0.25°. The daily mean of each parameter as well as the daily net heat fluxes were calculated as the sum of the daily means of each parameter: (Q_{net})=(Q_{sw})+(Q_{lw})+(Q_l)+(Q_s). B is positive when surface water gets lighter and negative when surface water becomes denser (river inputs as well as horizontal and vertical advection also contribute to density changes, but were not considered due to the lack of data).

[1] SSH_MED_SSH_L4_REP_OBSERVATIONS_010_021

3.1.8 Turner angle

The Turner angle (Tu) was computed to evaluate the relative roles of temperature and salinity gradients on the density gradients. Tu is defined as the four-quadrant arctangent [21], which units are degrees of rotation and was calculated with the Gibbs-SeaWater (GSW) Oceanographic Toolbox [22]. For the calculations, Argo float salinity and temperature were converted to absolute salinity and to conservative temperature (conservative temperature represents the heat content more accurately [22]), respectively.
$|Tu| < 45°$ indicates stable stratification, while $|Tu| > 90°$ characterizes a statically unstable water column (where the Brunt-Väisälä frequency $N^2 < 0$), with respect to both the temperature and salinity profile. $45° < Tu < 90°$ is called the salt finger regime, i.e. that the density gradient is mainly influenced by the salinity gradient, with the strongest activity near 90°; $-90° < Tu < -45°$ is called the diffusive regime, i.e. that the density gradient is mainly determined by the temperature gradient, reaching the strongest activity near $-90°$.

Chapter 4

Results

4.1 Argo float statistics of the Levantine Sea

4.1.1 Float speed and residence time

Argo floats drift with water masses at different programmed parking depths (PD), mainly at 350 m (intermediate waters) or 1000 m (deep waters). Therefore, the Argo float speed approximately gives the speed of intermediate and deeper water masses. Float speed and residence time are also useful for further float deployments: To obtain a good float coverage, the float deployments should take place in areas of low mean residence times, though not in areas of high numbers of lost floats, e.g. a float deployed at the beginning of the Asia Minor Current (latitude: $35° - 36°$, longitude: $34° - 35°$) could travel all the Levantine Sea, using its overall cyclonic circulation.

The frequency distribution of float speed, the corresponding data points and the total residence time of single floats for the two different parking depths within the area of the Levantine Sea from 2000 to 2017 are shown in Figure 4.1. The mean float speed at intermediate depths (PD=350 m) is 3.9 cm/s, while the mean float speed at deeper depths (PD=1000 m) is 2.9 cm/s.

Float deployments, lost floats, floats entering, floats leaving and number of float profiles for two different parking depths within the Levantine Sea from 2000 to 2017 are shown in Figure 4.2.
Total residence time, mean residence time, standard deviation of mean residence time, mean speed and standard deviation of mean speed are shown in Figure 4.3.
Most deployments (11) for PD=350 m took place in the area of Cyprus Eddy, while most deployments (8) for PD=1000 m took place in the area of RG. The highest float losses (13) for both parking depths occurred along the Southern Levantine coastline. The highest numbers of float entering and leaving occurred within the Cyprus Eddy for PD=350 m and within RG for PD=1000 m. This is due to highest numbers of

deployments in these areas and due to the anticyclonic and cyclonic nature of Cyprus Eddy and RG, respectively. The highest numbers of float profiles for PD=350 m are located within Cyprus Eddy and within Latakia Eddy (for position of eddies see Figure 1.4b) and for PD=1000 m within RG and Mersa-Matruh-Eddy.

The highest total residence times (700 days; circa 2 years) at PD=350 m occurred east to the island of Cyprus, within Cyprus and Latakia Eddy, while highest total residence times (1000 days; circa 2.7 years) at PD=1000 m were located within Rhodes Gyre. The highest mean residence time (170 days) at PD=350 m occurred within the 'wandering' Shikmona Eddy, while at PD=1000 m the highest mean residence times (200 days) were found within RG, Cyprus Eddy and Shikmona Eddy.
Highest mean speed for both parking depths were found along the Mid Mediterranean Jet (see Figure 1.4b).
From the $1° \times 1°$ plot of mean speed general features like the Mid Mediterranean jet (MMJ) can be seen. The $1° \times 1°$ plot of mean residence time shows that Levantine Deep Water (LDW) is trapped within the the two main circulation subsystems of the Levantine Sea (Rhodes Gyre, Cyprus Eddy) while the LIW is more influenced by the upper circulation.
The intermediate water within the Levantine Sea travels with a mean speed of about 3 cm/s (Figure 4.1). This equals (at latitude 35) to about 950 km per year or to about 10.4 longitudes per year (5.2 longitudes per half a year), assuming that the LIW follows a straight pathway. Intermediate water that was observed, e.g. at longitude 27, could have been formed half a year earlier e.g. at longitude 32 or at another formation place. Realistically, it takes much more time due to anticyclonic or cyclonic structures during the pathway of the intermediate water.

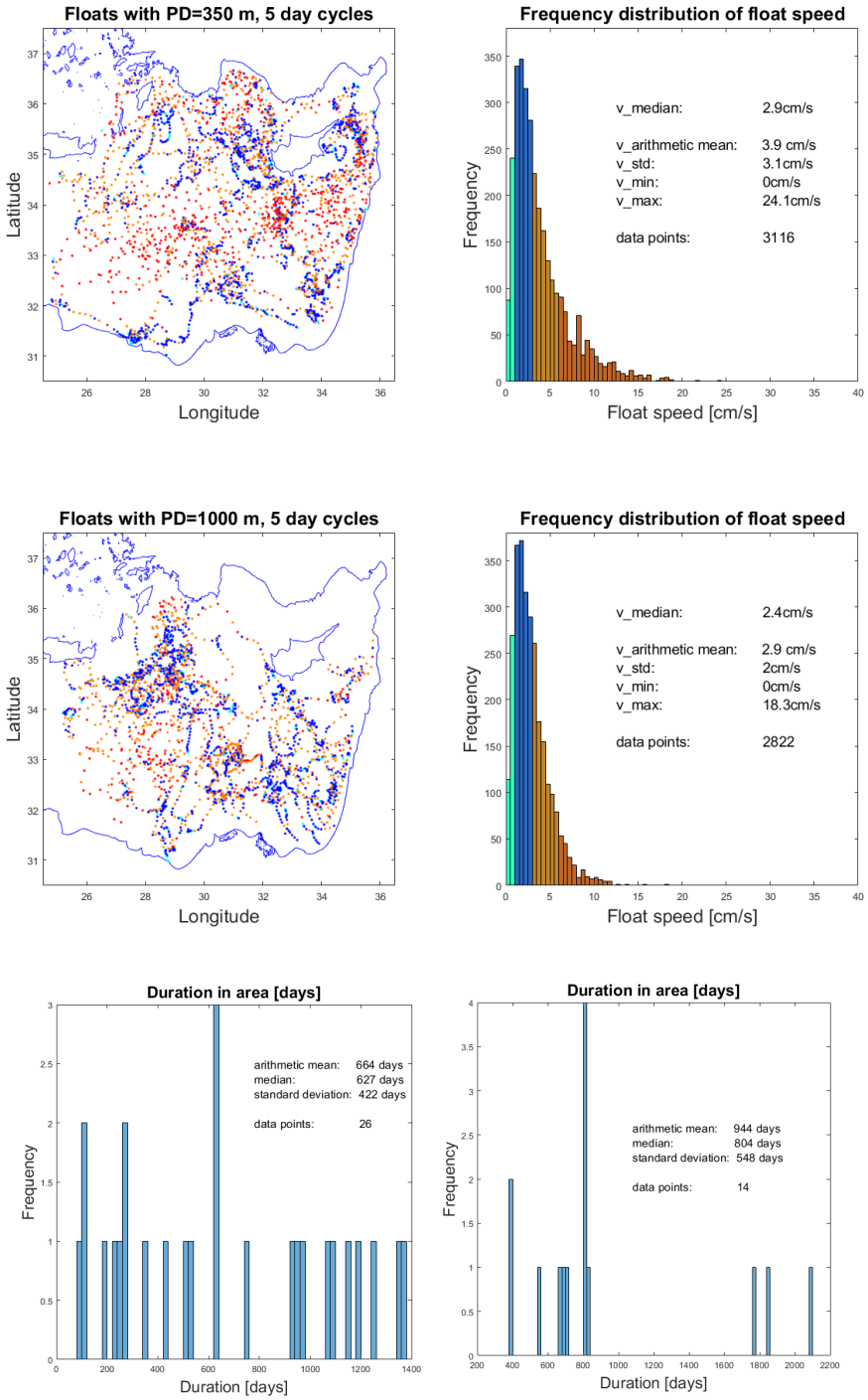

Figure 4.1: **Upper panel** left: Profile data points and associated speed with PD=350 m. Upper panel right: Frequency distribution of float speed (PD=350 m). **Central panel** left: Profile data points and associated speed with PD=1000 m. Central panel right: Frequency distribution of float speed (PD=1000 m). **Lower panel** left: Duration of stay of each float with PD=350 m within the area of the Levantine Sea. Lower panel right: Duration of stay of each float with PD=1000 m within the area of the Levantine Sea. From 2000 to 2017.

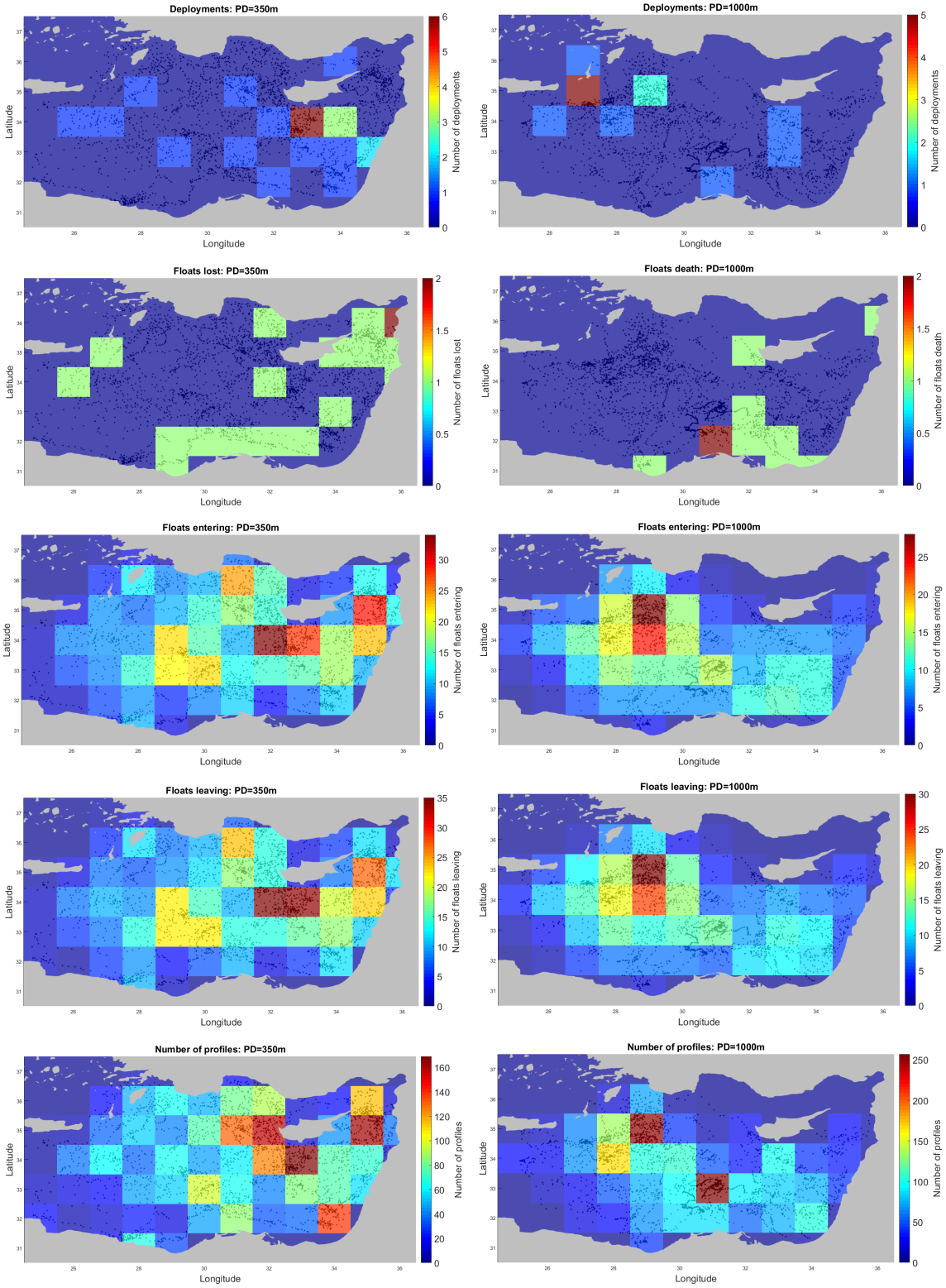

Figure 4.2: Float deployments, floats lost, floats entering, floats leaving and number of float profiles for PD=350 m (left panel) and for PD=1000 m (right panel) from 2000 to 2017.

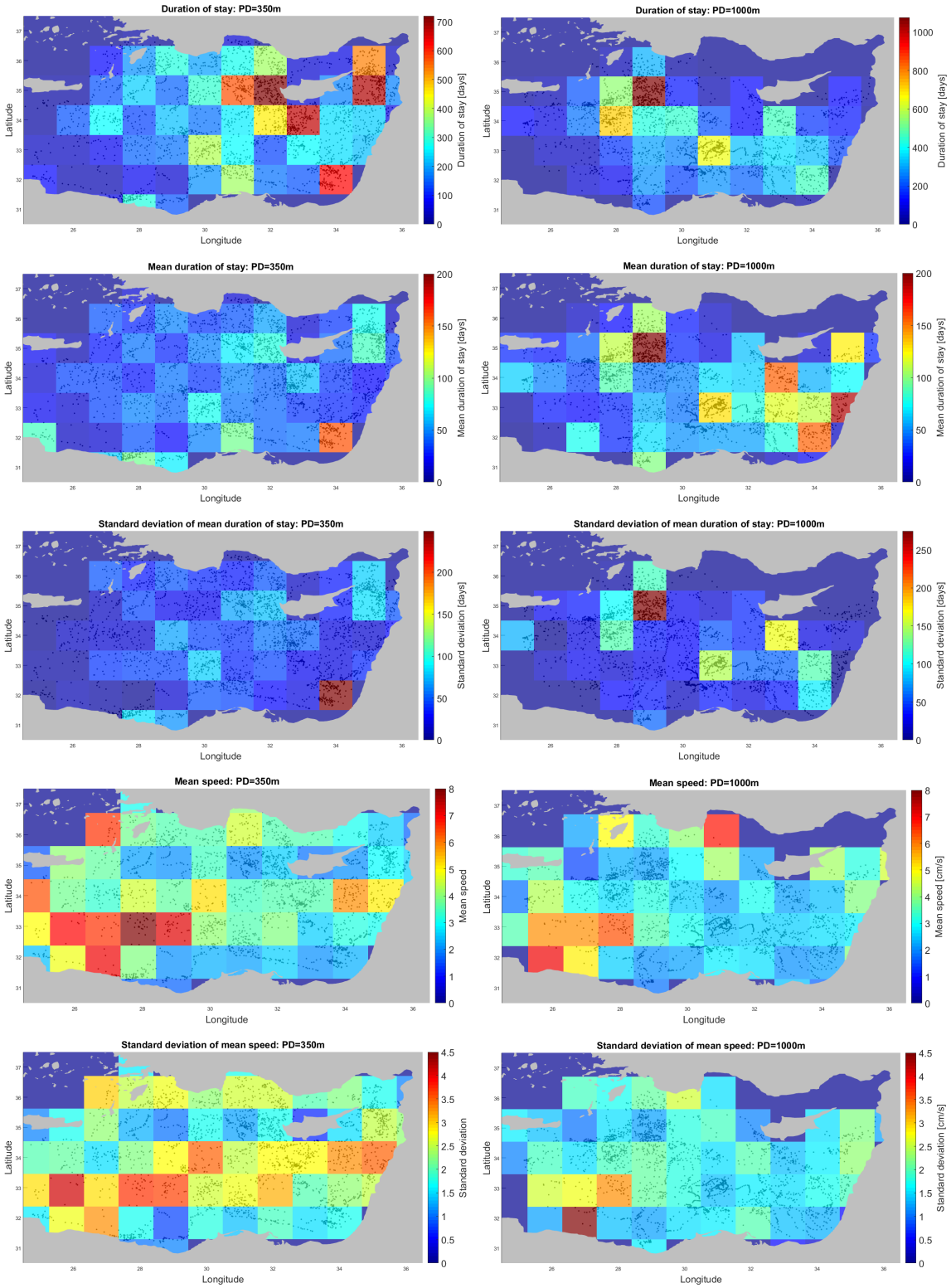

Figure 4.3: Total residence time, mean residence time, standard deviation of mean residence time, mean speed and standard deviation of mean speed for PD=350 m (left panel) and for PD=1000 m (right panel) from 2000 to 2017.

4.1.2 Mixed layer depth

The 1° × 1° climatologies of maximum mixed layer depth, winter maximum mixed layer depth, winter mean mixed layer depth and the standard deviation of the winter mean mixed layer depth for the area of the Levantine Sea from 2000 to 2018 are shown in Figure 4.4. The climatologies of maximum and winter maximum MLD are identical (Figure 4.4, upper panel), i.e. that the maximum MLDs occur during winter months. Deep dense water formation events are not indicated by the MLD climatology, due to the process of recapping (described in Section 3.1.5).
The 1° × 1° climatology of winter mean MLD indicates deepest MLDs within eddies and gyres (RG, IE, MME, CE, LTE; see Figure 1.4b for position of eddies) and along the Levantine coastline.

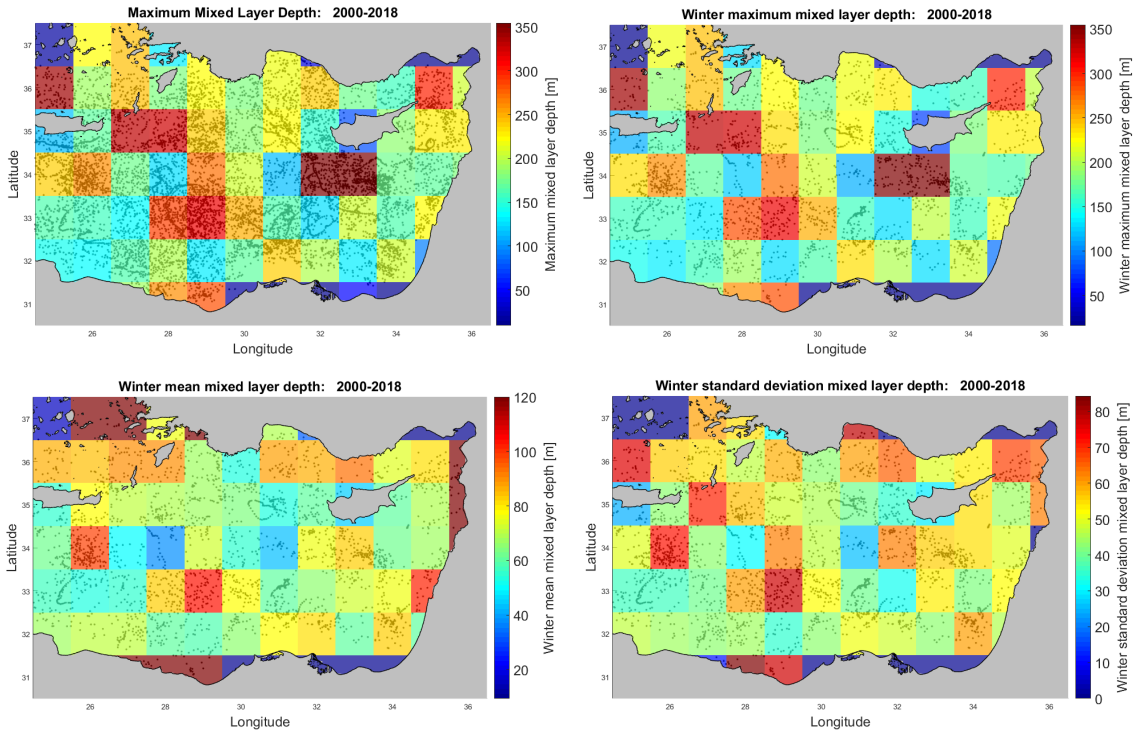

Figure 4.4: Maximum MLD, winter maximum MLD, mean winter MLD and standard deviation of mean MLD from 2000 to 2017 for PD=350 m (left panel) and for PD=1000 m (right panel).

4.1.3 Ocean heat content

The 1°×1° climatologies of the mean OHC for the area of the Levantine Sea from 2000 to 2017 are shown in Figure 4.5. The mean OHC was calculated for the entire water column (until a maximum depth of about 2000 m) below 0 and 50 m (Figure 4.5, upper panel) and below 100 and 500 m (Figure 4.5, central panel). The mean OHC is lowest in areas of net upwelling, i.e. in cyclonic structures such as RG and largest

in areas of net downwelling, i.e. in anticylconic structures such as Cyprus Eddy. The mean OHC<500 m (Figure 4.5, lower panel) shows strong net downwelling of warmer surface waters within Cyprus Eddy and along the Cretan Arch passage (as observed by analyzation of single Argo float profiles). Also the influence of the anticyclonic EE, MME and IE (see Figure 1.4b for position of eddies) on deeper layers (<500 m) can be seen.

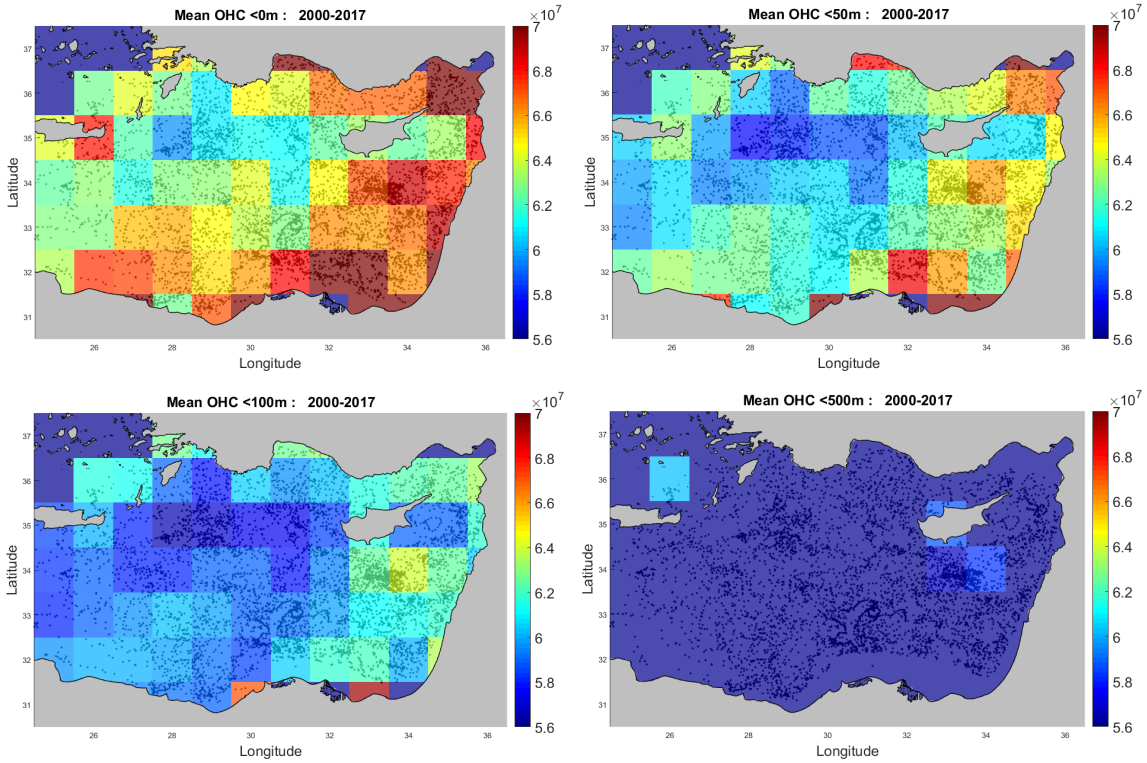

Figure 4.5: Upper panel: Mean OHC (J)<0 m, mean OHC (J)<50 m; lower panel: Mean OHC (J)<100 m, mean OHC (J)<500 m

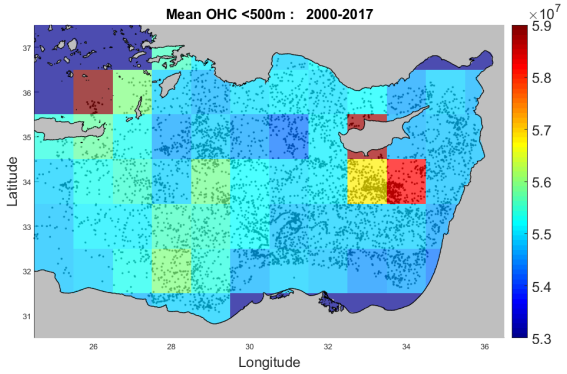

Figure 4.6: Climatology of the mean OHC<500 m

4.2 Levantine intermediate and deep water formation

4.2.1 Buoyancy, heat and freshwater fluxes within the Northwestern Levantine Sea

Dense water formation events depend mainly on the surface buoyancy fluxes B, which in turn depend on the heat fluxes through the air-sea interface, scaled by the thermal expansion coefficient α, and the freshwater fluxes, scaled by the haline contraction coefficient β. Monthly surface buoyancy fluxes and their thermal and haline (freshwater) components, integrated over the center of RG (longitude: 28-31 °E, latitude: 34-36 °N), are shown in Figure 4.7.

The upper panel of Figure 4.7 shows the thermal buoyancy fluxes, while the lower panel shows the haline and the total buoyancy fluxes. The dense water formation events (Figure 4.7 (blue and yellow circles); Table 4.1), captured by the Argo floats (Table 4.2), occurred *after* maxima of the haline buoyancy fluxes, i.e. after the highest evaporation took place, and *during* minima of the thermal buoyancy fluxes, i.e. during maximum heat losses.

The haline buoyancy flux is one order larger than the thermal buoyancy flux and dominates the surface buoyancy fluxes (Figure 4.7, Lower Panel). The total buoyancy flux is negative, therefore the RG is an area of net buoyancy loss, driven by the haline component.

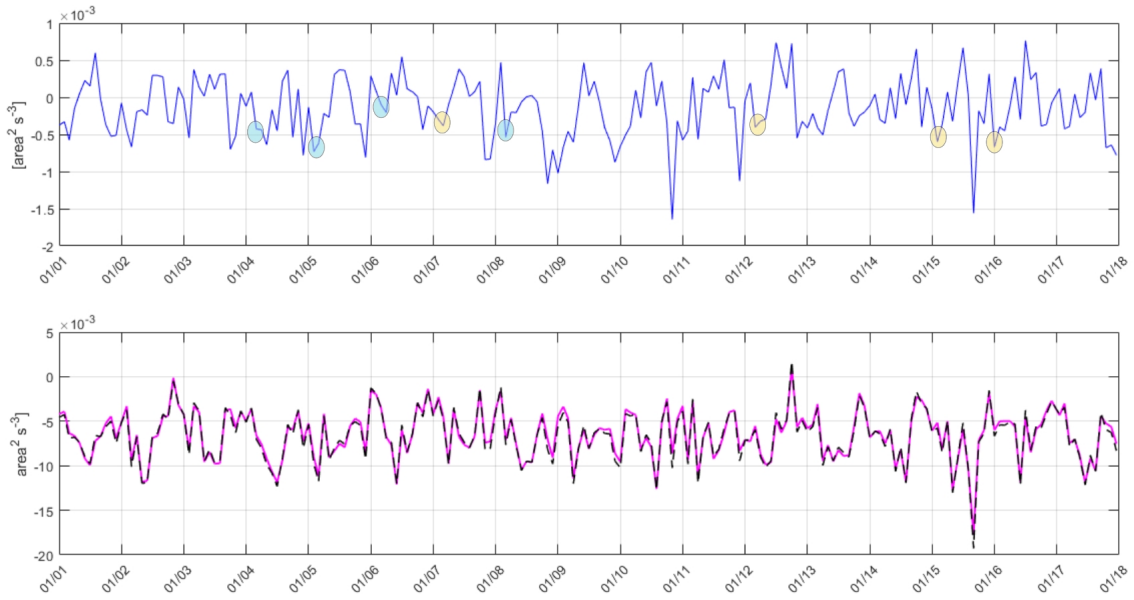

Figure 4.7: Upper panel: Time series of the monthly thermal component (B_T) from 2001 to 2017, integrated over the center of RG (longitude: 28-31°E, latitude: 34-36°N). Blue and yellow circles indicate events of pronounced dense water formation detected by the Argo floats within RG and along the coastline, respectively (Table 4.1). Lower panel: Time series of the monthly haline component (B_S; magenta line) and buoyancy fluxes (B; black dotted line).

Table 4.1: Pronounced (mixed layer depth (MLD) >250 m) dense water formation events within the center of RG and along the Northern coastline: Area of formation, float WMO, time period, watermass characteristics, and maximum depth during the dense water formation events.

Area of Formation	**Float WMO**	**Time Period**	**Water Mass Characteristics**	**Maximum Depth**
RG	6900098	FM 2004	LDW	At least 600 m, probably 1000 m [1]
RG	6900098	FM 2005	LDW	At least 600 m, probably 1000 m [1]
RG	6900098	JF 2006	LDW	At least 600 m, probably 1000 m [1]
RG	6900098	FM 2008	LDW	At least 600 m, probably 1000 m [1]
COAST	6900098	M 2007	LIW	About 550 m
COAST	6900843	FM 2012	LIW	About 350 m
COAST	6901824	FM 2015	LIW	About 350 m
COAST	6901868	FM 2016	LIW	About 300 m

[1]T-S plots show the formation of dense water with a potential density that corresponds to the density of the upper deep boundary layer which is found at approximately 1000 m depth.

Table 4.2: Argo floats capturing pronounced (MLD>250 m) dense water formation events.

Float Number	**Float Description**
WMO 6900098	Apex Profiling Float, Naval Oceanographic Office (NAVO). Alive from 20.07.2003 to 19.04.2009, lifetime approximately 5 years, Parking depth (PD)=1000 m, 5 day cycle.
WMO 69000843	Apex Profiling Float, Argomed, Euro-Argo. Alive from 03.10.2011 to 31.05.2014, PD=350 m, 5 day cycle.
WMO 6901824	Arvor Profiling Float, Argo Italy, Argomed, Euro-Argo. Alive from 04.11.2013 to 03.02.2018, PD=350 m, 5 day cycle.
WMO 6901868	Apex Profiling Float, Argo Italy, Euro-Argo. Alive from 01.12.2014 to 29.07.2017, PD=350 m, 5 day cycle.

The climatology of monthly heat fluxes Qnet for the center of RG from 2001 to 2017 shows that the largest heat losses which induce the preconditioning phase occurred mainly in November and in December (Figure 4.8). The subsequent heat losses in JFM induce the formation of dense water and therefore lead to convection and mixing.

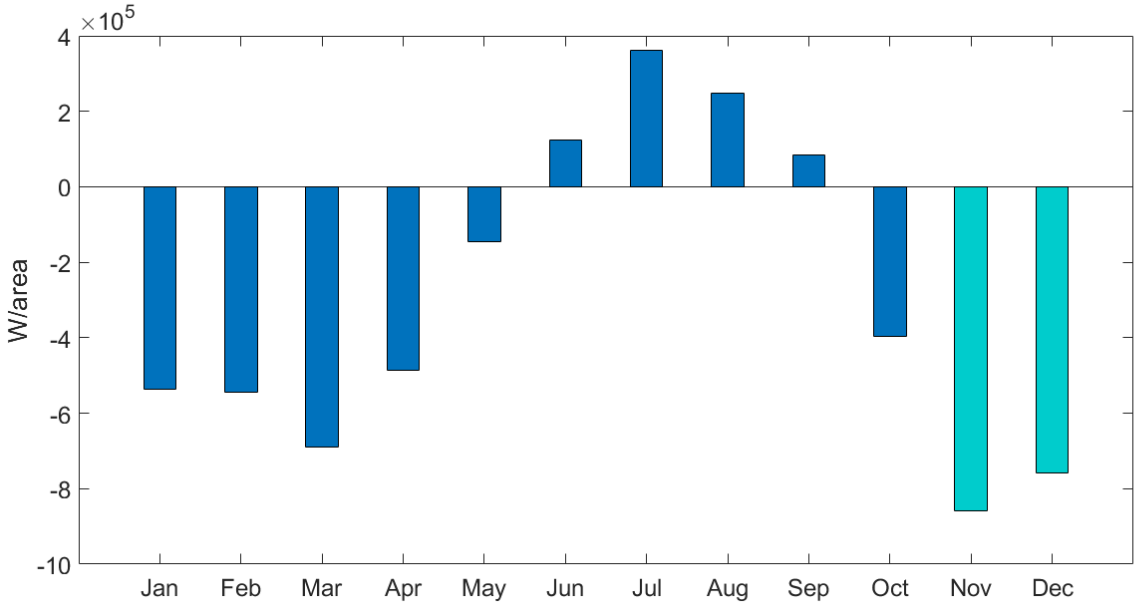

Figure 4.8: Climatology of monthly heat fluxes from 2001 to 2017, integrated over the center of RG (longitude: 28-31°E, latitude: 34-36°N). Main heat losses generally occur in November and December (turquoise bars) and initiate the preconditioning phase. Subsequent heat losses in January, February, and March induce dense water formation.

4.2.2 LIW and LDW Formation within the Northwestern Levantine Sea

Intermediate and deep water formation events in the NWLS (latitude: 33-37 °N, longitude: 26-32 °E) were analyzed during the winter months (JFM) from 2001 to 2017 (879 T/S profiles from 20 floats). Most of the float profiles within the NWLS showed regular winter MLDs, i.e., MLDs between 100 and 200 m. Pronounced dense water formation, i.e., with a MLD deeper than 250 m, occurred only within the center of RG, along the Northern coastline and along the Cretan Arch passage. Events of pronounced LDW (13.7 ℃<potential temperature<14.5 ℃, 38.8 psu<salinity<38.9 psu) and 'lower range' LIW (potential temperature around 15 ℃ and salinity around 39 psu) formation were detected within the center of RG in winter 2004, 2005, 2006, and 2008 and events of pronounced LIW formation (potential temperature>15 ℃ and salinity>39 psu) were detected along the Northern coastline in winter 2007, 2012, 2015 and 2016 (Table 4.1). More than 800 profiles of 20 floats were analyzed, but only four floats (Table 4.1,4.2) captured pronounced dense water formation, being at the right place at the right time. To document the dense water formation events the float had to be either inside or pass later through the area of dense water formation. Float WMO 6900098 had an exceptionally long lifetime of nearly 6 years and therefore it was able to capture one event of pronounced LIW formation along the Northern coastline and four events of pronounced DWF. Unfortunately, it stopped measuring at 600 m depth. The WMO numbers of the Argo floats that found pronounced dense water formation events within the center of RG and along the coastline are listed in Table 4.2.

4.2.2.1 LDW formation within the Rhodes Gyre

Two examples of LDW formation within RG are given in this subsection.

(1) In JFM 2006, float WMO 6900098 was entrapped in the center of RG (Figure 4.9a). Hoevmueller plots of salinity, potential temperature, and potential density describe two pronounced events of mixing and convection during this winter (Figure 4.9b,c,d). The first event occurred by the end of January until mid-February and led to LDW formation (13.7 ℃<potential temperature<14.5 ℃, 38.8 psu<salinity<38.9 psu) while the second event around mid-March led to LDW and 'lower range' LIW (temperature about 15 ℃ and salinity about 39 psu) formation.
In December, very high surface salinity values (S>39.15 psu) were detected in the upper 50 m (Figure 4.9b). However, mixing and convection is still prevented by relatively high surface temperatures during December. The surface temperature has a decreasing trend from 17.5 ℃ by the beginning of December to 15.5 ℃ in early

January and reached a minimum of about 14 ℃ from the end of January to the end of February.

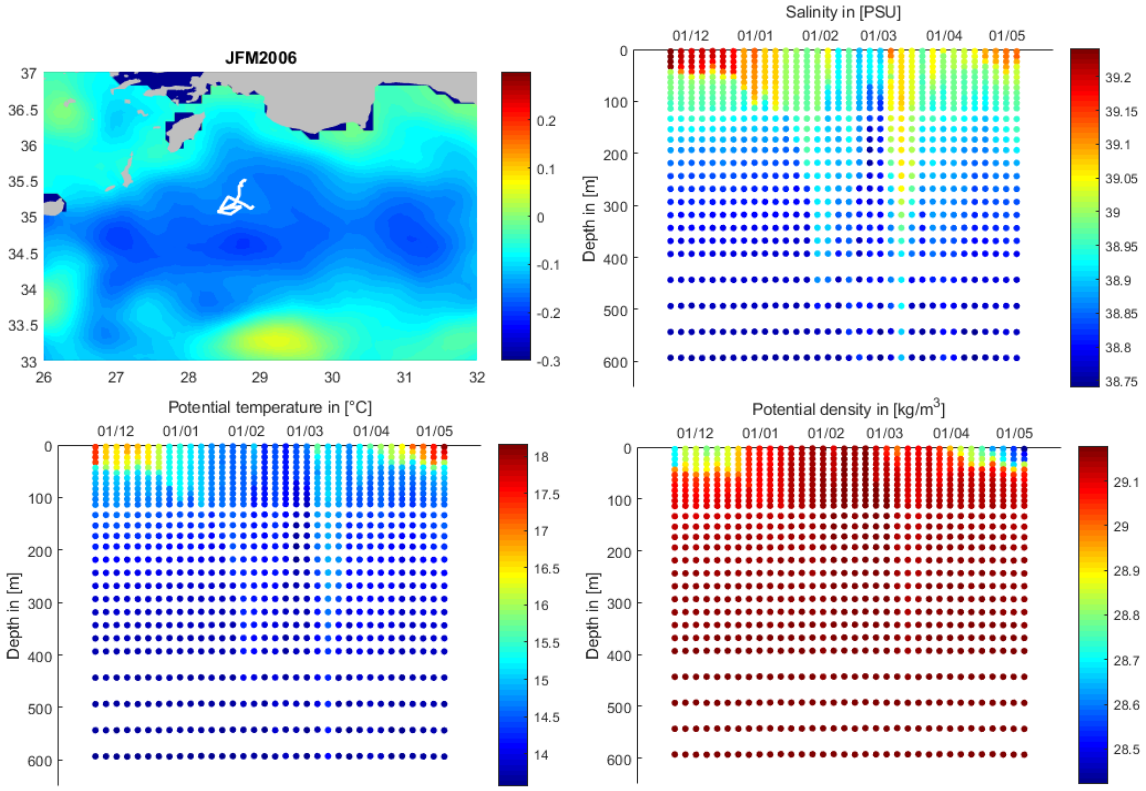

Figure 4.9: Upper panel: Left: Mean sea surface height (SSH, m) and float trajectory of float WMO 6900098 for JFM 2006; Right: Salinity (PSU). Lower panel: Left: Potential temperature (℃) and Right: potential density (kgm^{-3})

From the beginning of March, the surface temperature gradually increased, reaching 15.5 ℃ during March with a successive increase to 17.5 ℃ by the end of April. The MLD deepens from 50 m within December to about 100 m in the beginning of January and the high surface salinity is mixed to intermediate layers.
By the end of January, when lowest surface temperatures (T=14-14.5 ℃) are reached, dense water formation starts to occur. Potential density reaches its highest values (29.1 kgm^{-3}) by the end of January until mid-February and the examination of single profiles shows that deep convection takes place down to at least 600 m during this period.

The Hoevmueller plot of the Turner angle (Figure 4.10) reveals statically unstable conditions (|Tu|>90 °; dark blue and dark red points) from mid-January to the end of March and indicates the deep dense water formation events down to at least 600 m in February and March 2006. The deep dense water formation events are characterized by a stronger contribution of temperature (-45 °<Tu<-90 °; blue points), while the

main contributor to the stable stratification in December and April is mainly the salinity (45 °<Tu<90 ° ; yellow and light orange points).

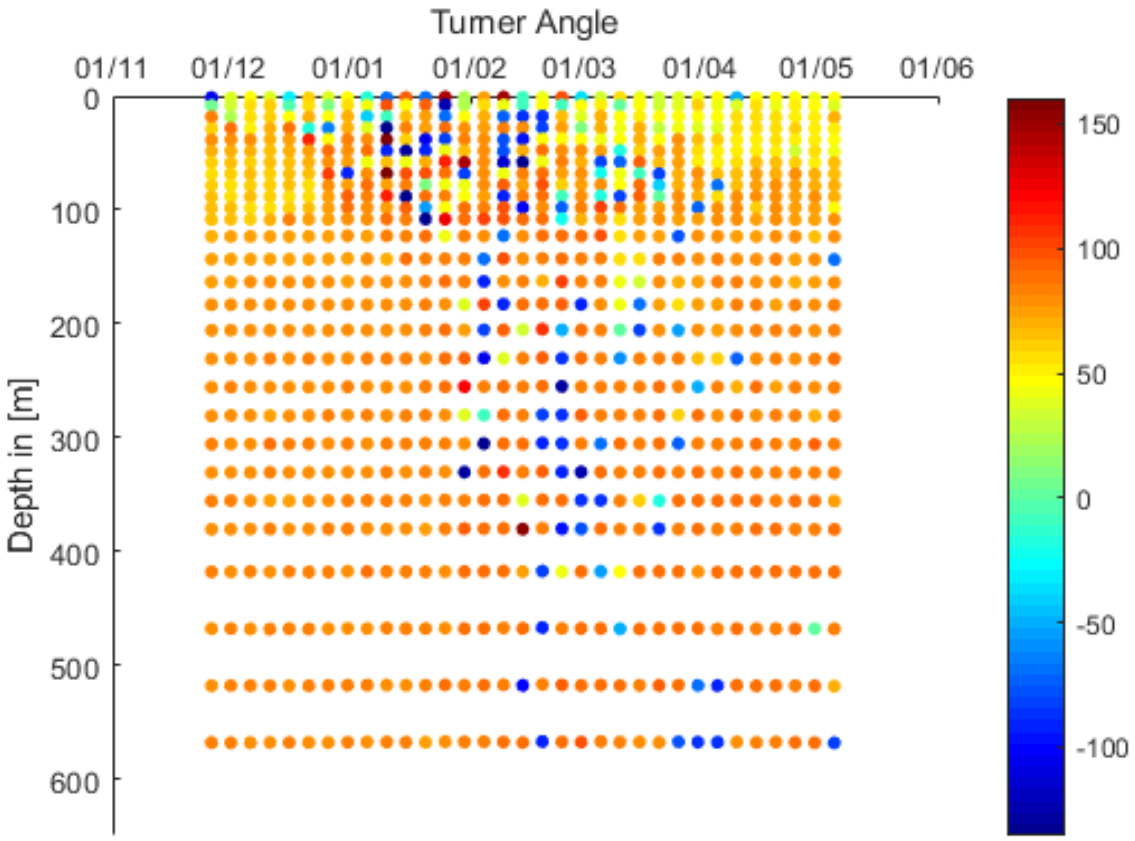

Figure 4.10: The Turner angle (°) of float WMO 6900098 describes the contribution of salinity and temperature gradients to the density gradient.

The heat and freshwater fluxes, integrated over the center of RG, show an intense preconditioning phase during December 2005, due to strong dry and cold winter winds which led to heat losses (Figure 4.11a) and evaporation (Figure 4.11b) and consequently to high surface salinity values. Additional heat losses by the end of January and the beginning of February coincide with the LDW formation event within the RG described above. The heat losses in mid-March coincide with the second dense water formation event within RG which led to a mixture of LDW and 'lower range' LIW formation.

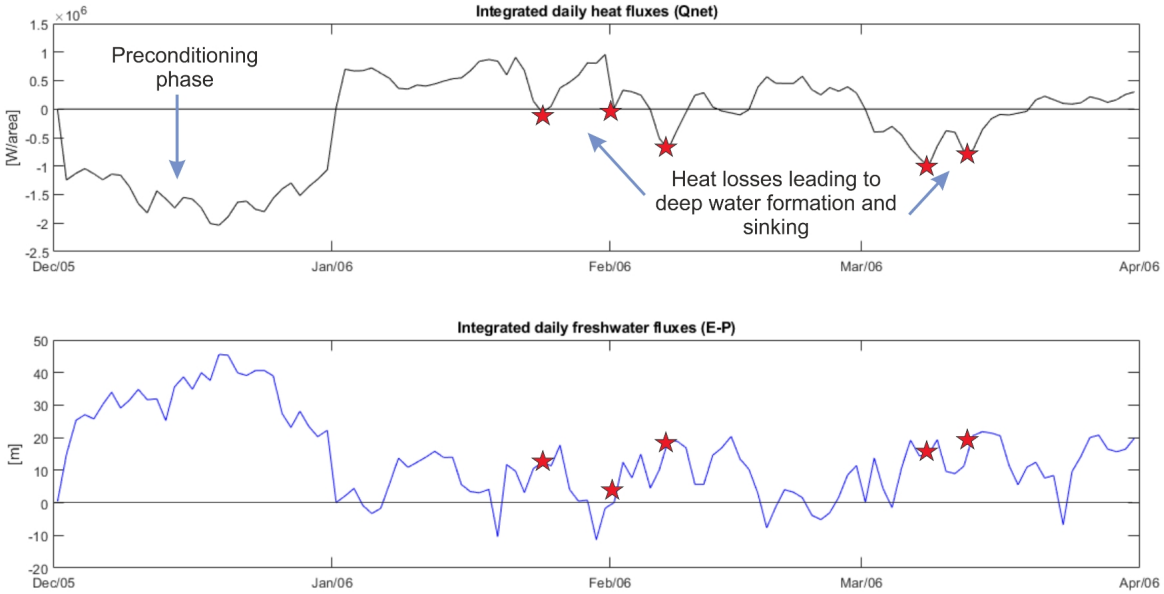

Figure 4.11: **Upper panel:** Time series of daily surface heat fluxes from December 2005 to April 2006, integrated over the center of RG (longitude: 28-31°E, latitude: 34-36°N). The heat losses by the end of January and mid-February induced deep convection and formation of Levantine deep water (LDW) while the heat losses in March induced mixing and formation of LDW and 'lower range' LIW (see also Figure 4.9). **Lower panel:** Time series of daily freshwater fluxes from December 2005 to April 2006, integrated over the center of RG (longitude: 28-31°E, latitude: 34-36°N). The freshwater fluxes in December show a strong evaporation which led to increased surface salinity as shown by Argo float data (Figure 4.9b).

This deep convection event from the end of January until mid-February coincides with a strong depression of SSH within the RG area during that time, overlapping the exact position of the float (longitude: 28.5-29°E, latitude: 35-35.5°N ; Figure 4.12). Figure 4.12a shows the float trajectory and mean SSH of January, February, and March 2006 while Figure 4.12b,c,d show the negative daily SSH and geostrophic currents for three specific days during the period of deep convection event from the end of January to mid-February. The eddy in which the float was trapped, represents the strongest depression (SSH<-0.3 m; about 20 cm below the seasonal mean (Figure 4.12a)) during winter months reaching a negative maximum during the days of deep water formation (Figure 4.12b,c,d). The mesoscale eddy during that time shows a diameter of about 60 km which is within the typical mesoscale eddy diameter within the Levantine Sea (40-80 km).

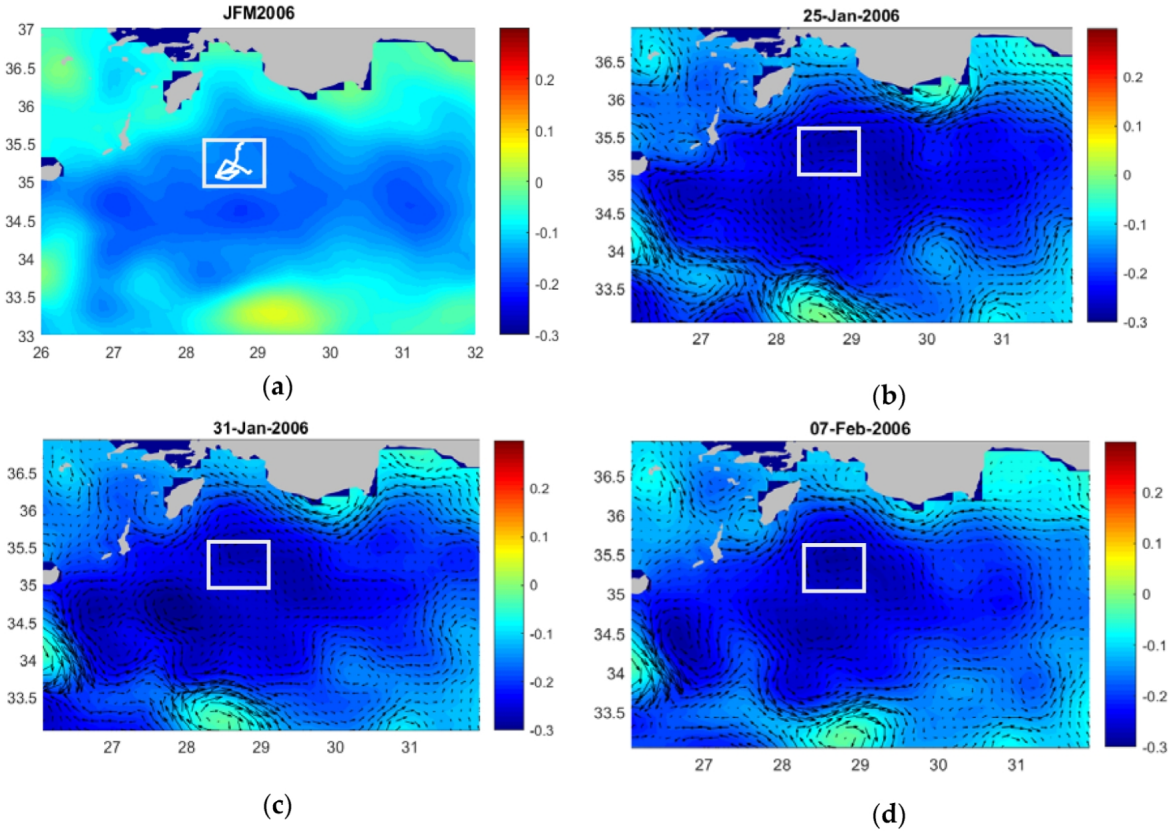

Figure 4.12: **a)** Trajectory of float WMO 6900098 depicted within the white rectangle, overlaid on mean SSH (m) for JFM 2006 for the NWLS. **b-d)** daily SSH (m) during the LDW convection events (from 25 January to 7 February 2006). The mesoscale eddy within the white box has a diameter of about 60 km.

Figure 4.13 shows the monthly means of satellite SST superimposed on the geostrophic currents derived from SSH. The deep convection event occurred by the end of January until mid-February 2006 when the sea surface temperature was lowest. The lowest surface temperatures measured by the Argo float, evidenced within the Hoevmueller plots (Figure 4.9c), coincide with lowest temperatures by daily satellite SST (Figure 4.13e,f) and with the strongest depression of SSH (Figure 4.12b-d) by the end of January until mid-February.

Figure 4.14 shows the T/S plots for the two events of dense water formation during JFM 2006. Water masses above 100 m were not taken into account for the T/S plot to exclude shallow MLDs and recapping and to capture the events of pronounced intermediate and deep water formation. Water masses from 100 to 500 m are plotted with a green dot while water masses under 500 m are plotted with blue dots.

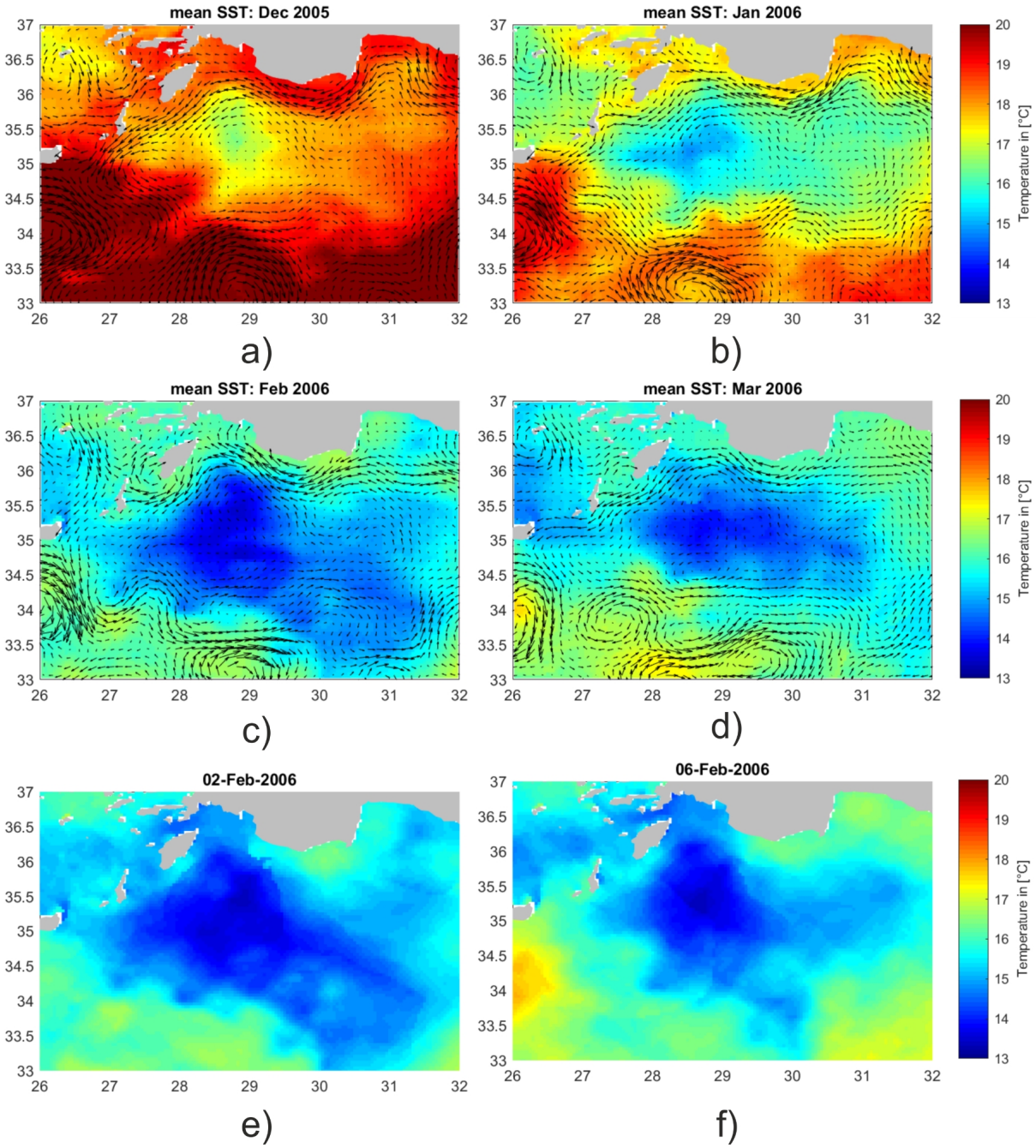

Figure 4.13: Monthly means of sea surface temperature (SST, ℃) and geostrophic currents for **a)** December 2005, **b)** February, **c)** February and **d)** March 2006. Daily SST (℃) of **e)** 2 February 2006 and **f)** 6 February 2006. Dense water formation and the deep convection event occurred by the end of January until mid-February when SST was lowest.

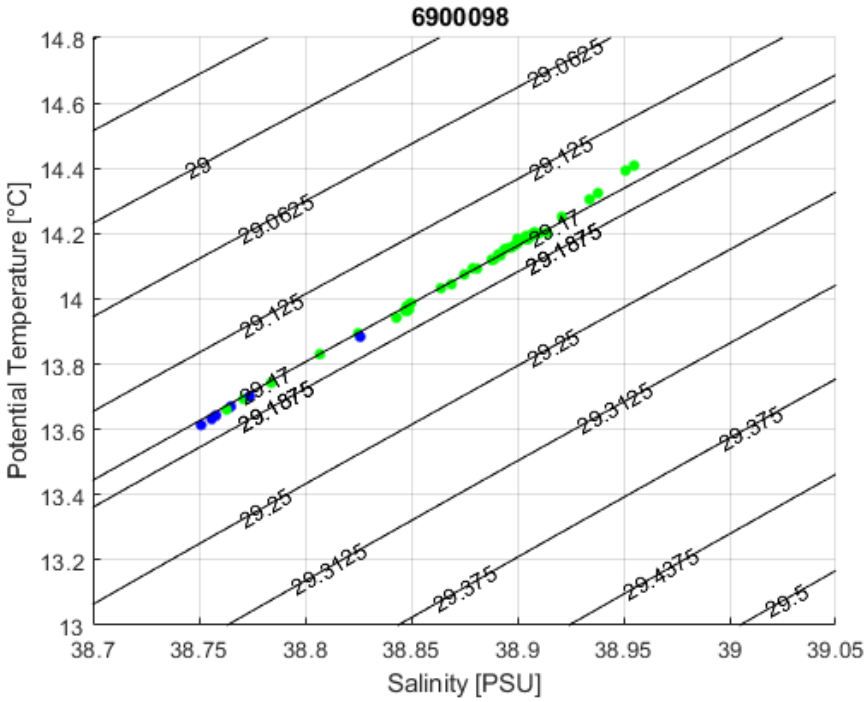

(a)

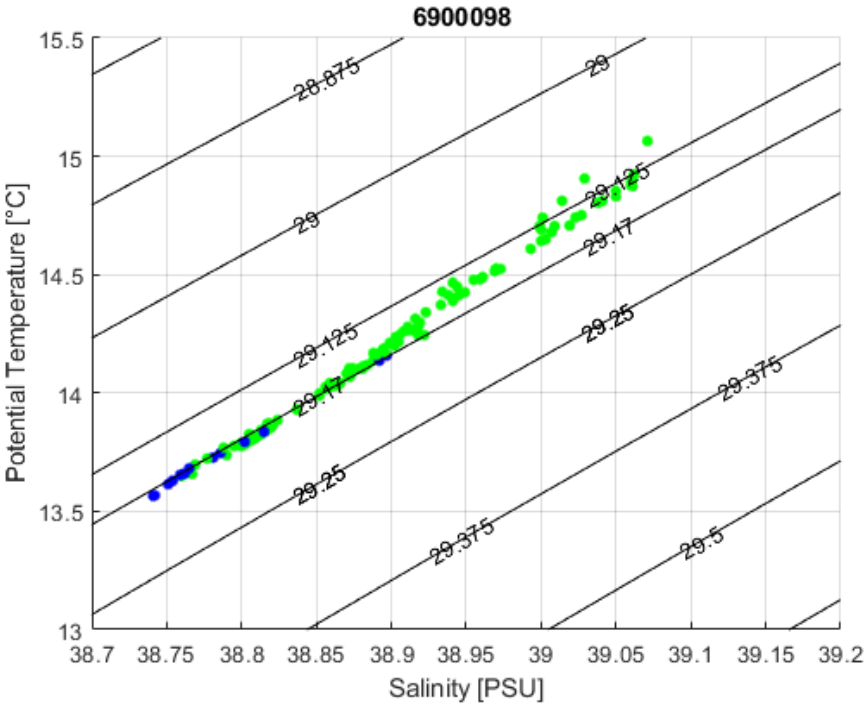

(b)

Figure 4.14: **(a)** The temperature and salinity (T-S) plot for float WMO 6900098 from 20 January to 20 February 2006 indicates LDW formation. The additional density line with a potential density value of 29.17 kgm^{-3} shows the upper deep-water boundary density which corresponds to approximately 1000 m depth for the NWLS [8]. **(b)** T-S plot for float WMO 6900098 for March 2006 indicates a mixture of LDW and 'lower range' LIW formation. Green dots represent depths from 100 to 500 m, while blue dots represent depths from 500 to 600 m.

Figure 4.14a shows the T/S plot for the first dense water formation event: The potential temperature exhibits values smaller than 14.5 ℃, the salinity shows values smaller than 39 psu, and the potential density shows a constant value of about 29.17 kgm^{-3}. The typical ranges for LDW for potential temperature are between 13.7 ℃ and 14.5 ℃ and for salinity between 38.8 to 38.9 psu [9, 16, 17]. The potential density line of 29.17 kgm^{-3} represents the upper deep-water boundary density for the NWLS, corresponding to approximately 1000 m depth [23]. All potential temperatures and salinity values lay on the line of constant potential density of 29.17 kgm^{-3}, i.e., that the formed water masses sank to at least 1000 m, until the same potential density was reached. Therefore, the T/S plot confirms that LDW took place during the first event by late January until mid-February (Figure 4.14a). For the dense water formation event in March 2006, the T/S plot shows potential temperatures smaller than 15 ℃, salinities smaller than 39.1 psu, and potential densities between 29.125 kgm^{-3} and 29.17 kgm^{-3}. By nearly reaching 15 ℃ and with some salinity values above 39 psu, a part of the water mass reaches the lower range of LIW water mass characteristics (Figure 4.14b). This indicates a mixture of LDW and 'lower range' LIW formation during the second dense water formation event within RG.

(2) LDW formation took also place from the end of February until mid-March 2004 within another cyclonic mesoscale eddy located in the western part of the RG. Hoevmueller plots for DJFMA for salinity, potential temperature, and potential density are shown in Figure 4.15. During January and February, the MLD deepens constantly and the event of LDW formation occurs by the end of February until mid of March when the minimum surface temperature was reached. The examination of single profiles shows convection down to at least 600 m.

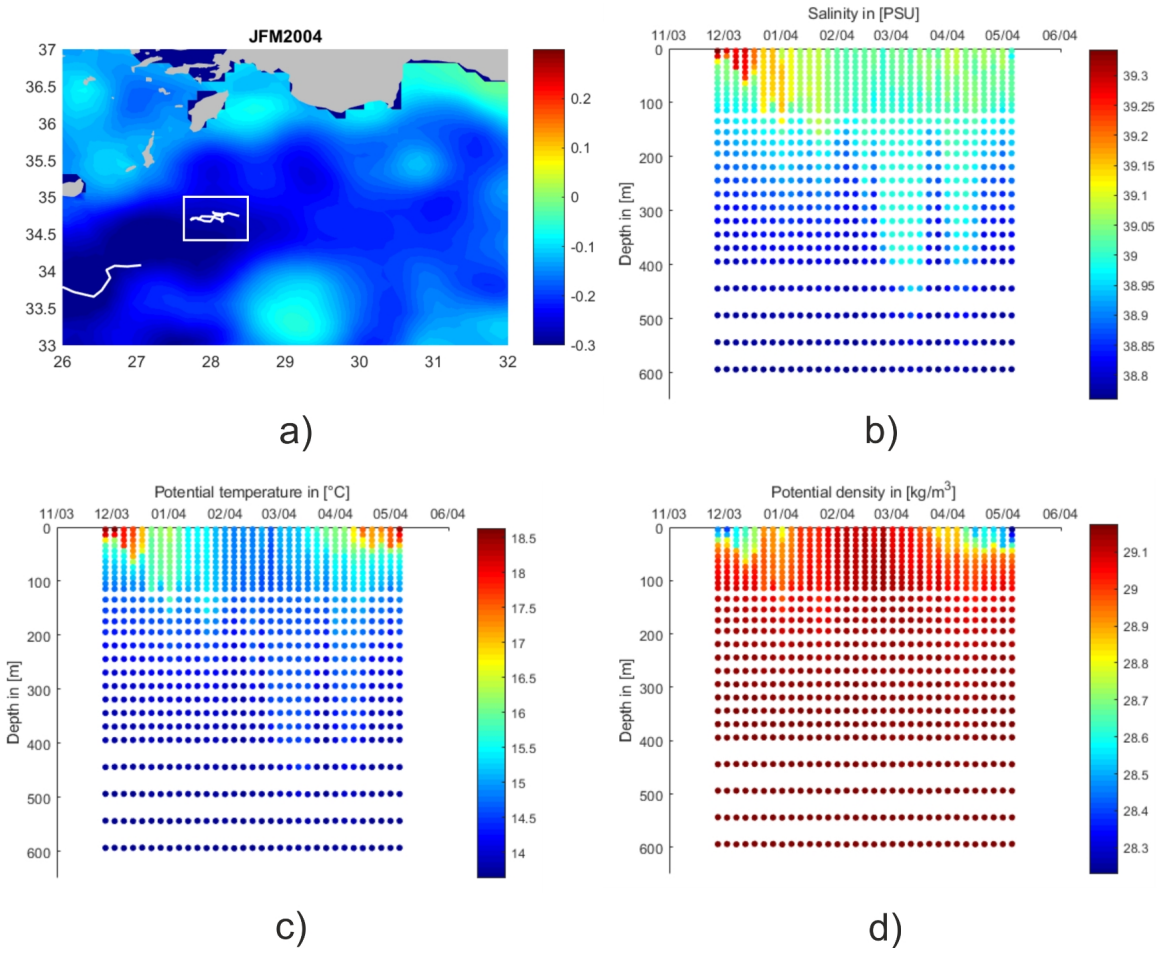

Figure 4.15: **a)** Mean SSH (m) of the Northwestern Levantine Sea and float trajectory of float WMO 6900098 for JFM 2004 (white rectangle). **b)** Salinity (PSU), **c)** potential temperature (°C), and , **d)** potential density (kgm^{-3}) from December 2003 to April 2004.

The Hoevmueller plot of the Turner angle (Figure 4.16) reveals statically unstable conditions (|Tu|>90 °; dark blue and dark red points) and therefore a continuous deepening of the MLD from mid-January to mid-March 2004 and indicates the deep dense water formation events down to 400 m by the end of February and mid-March. The main contributor to the stable stratification in December and April is the salinity (45 °<Tu<90 ° ; yellow and light orange points), while the deep dense water formation

events are also characterized by a stronger contribution of temperature gradients (-45 °<Tu<-90°; blue points). Salt-fingering (45 °<Tu<90 °; yellow points) can be noticed at a depth of about 350 m.

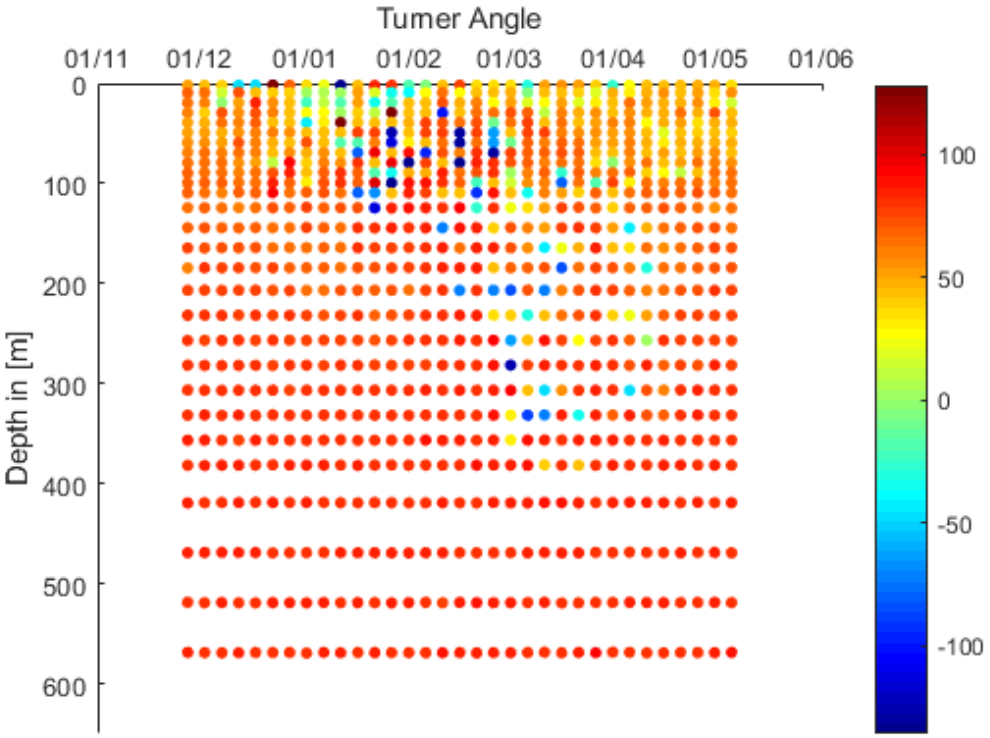

Figure 4.16: The Turner angle (°) of float WMO 6900098 shows the contribution of salinity and temperature gradients to the density gradient.

The T/S plot of JFM2004 shows mainly LDW formation (Figure 4.17). Green dots represent water masses between 100 and 500 m while blue dots represent water masses between 500 and 600 m. The water mass characteristics show LDW and lower range LIW (potential temperature around 15 ℃ and 39 psu<salinity<39.1 psu) formation.

Figure 4.18 shows: a) the mean SSH for JFM 2004 and the float trajectory (longitude: 27.5 °E-28.5 °E, latitude: 34.5 °N-35 °N) during this period and daily SSH b) before; c) during; and d) after the convection event. A strong powerful structure develops by mid-February with a negative SSH of more than -0.3 m. Analysis of single profiles shows that on 8 March 2004, a MLD down to about 450 m was formed while on the surface recapping already took place (newly formed MLD of about 80 m).

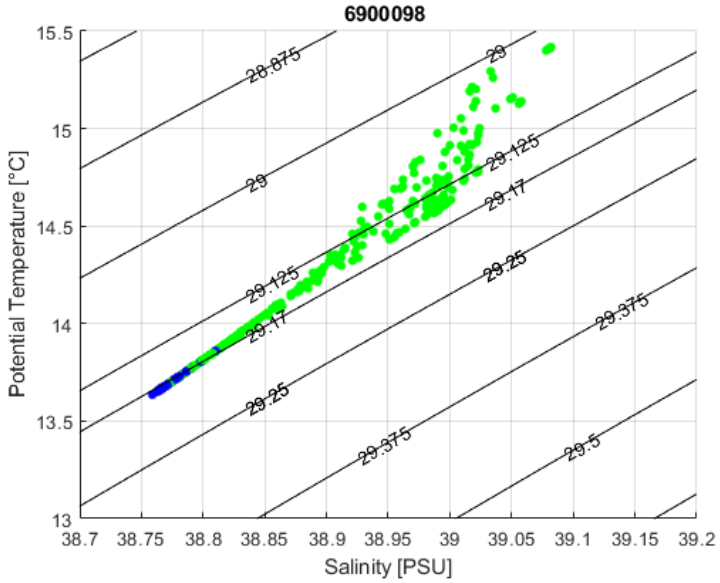

Figure 4.17: T-S plot for float WMO 6900098 for JFM 2004. Green dots represent depths from 100 to 500 m while blue dots represent depths from 500 to 600 m.

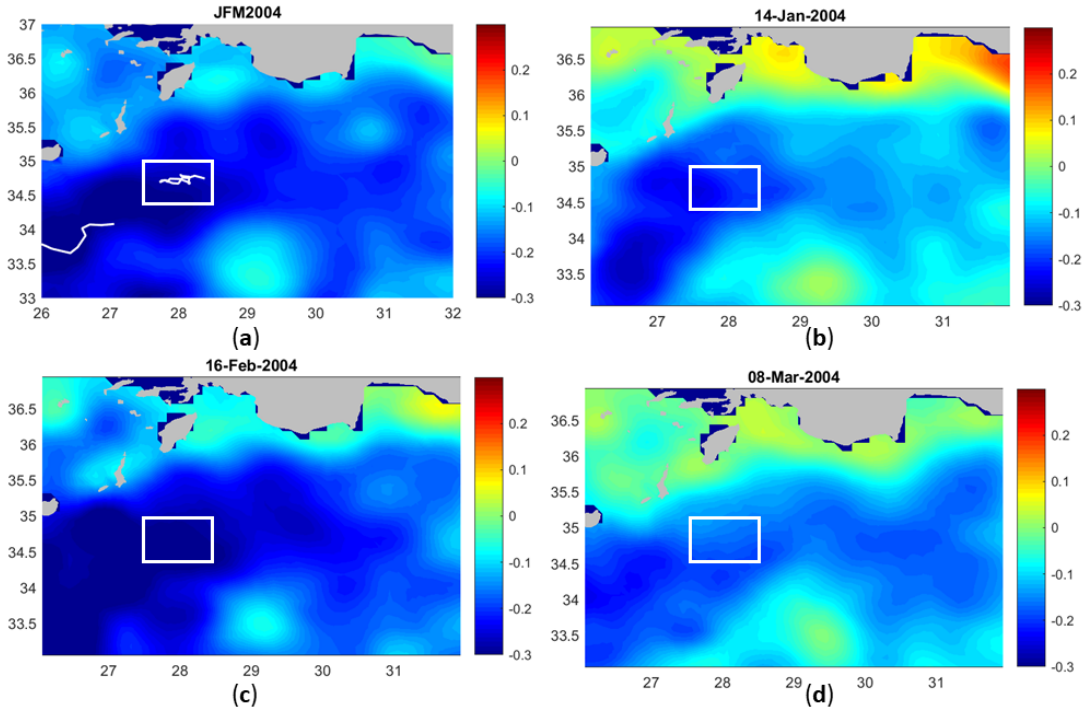

Figure 4.18: **a)** Mean SSH (m) for JFM 2004 and float trajectory of float WMO 6900098 (white rectangle). **b)** SSH (m) for the 14 January 2004; float profiles show 'regular' winter MLDs around 150 m. **c)** SSH (m) for the 16 February 2004; float profiles reveal dense water formation to about 350 m; **d)** SSH (m) for 8 March 2004; recapping with a newly formed MLD of about 80 m occurred, while the dense water formation event down to 450 m is still captured by the float profile.

Monthly means of satellite SST are shown in Figure 4.19. The satellite SST reached a minimum between mid-February and mid-March, i.e., during the event of deep water formation, and coincides with the surface potential temperature measured by the Argo float (Figure 4.15).

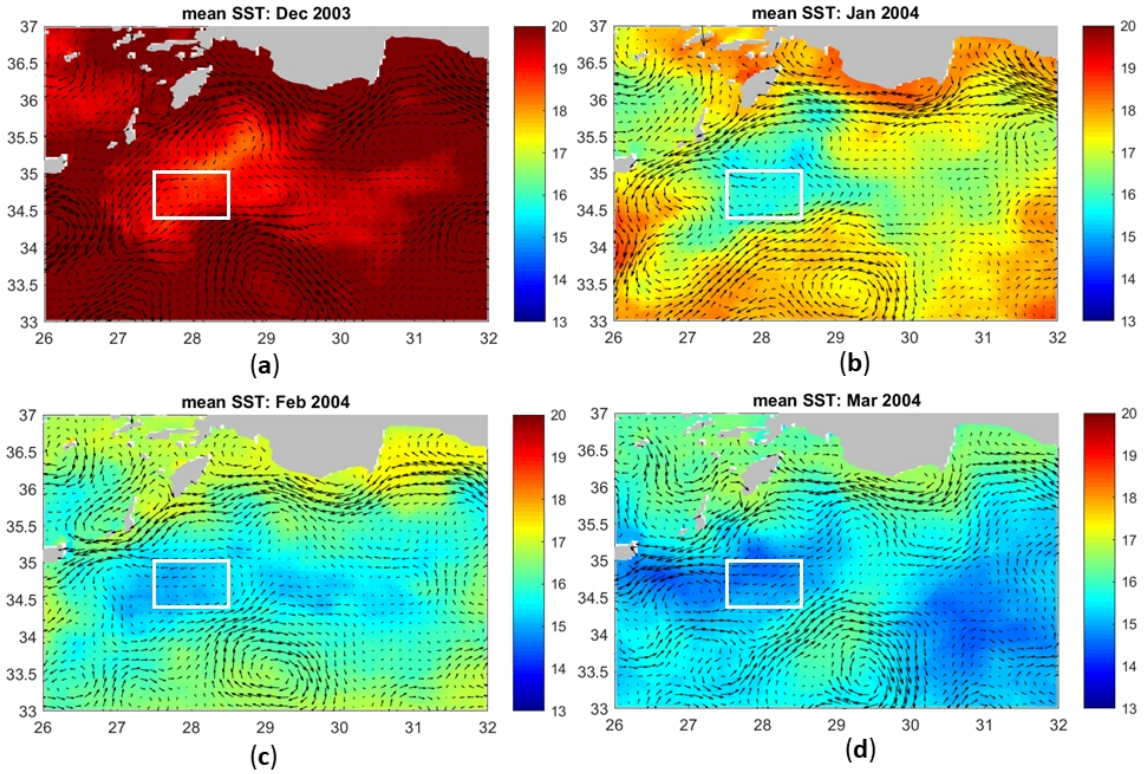

Figure 4.19: Monthly means of the satellite SST (°C) and absolute geostrophic currents from December 2003 to March 2004. The deep convection event occurred by the end of February and beginning of March 2004 when SST was lowest. The white rectangle shows the position of float WMO 6900098 during JFM 2004.

4.2.2.2 LIW formation along the coastline

One example of LIW formation along the coastline is given in this subsection.

While LDW was formed inside RG, typical LIW was instead formed along the Northern Turkish coastline, i.e., along the AMC. The salinity, potential temperature, and potential density values characterize a typical LIW formation event by the end of March (Figure 4.20).

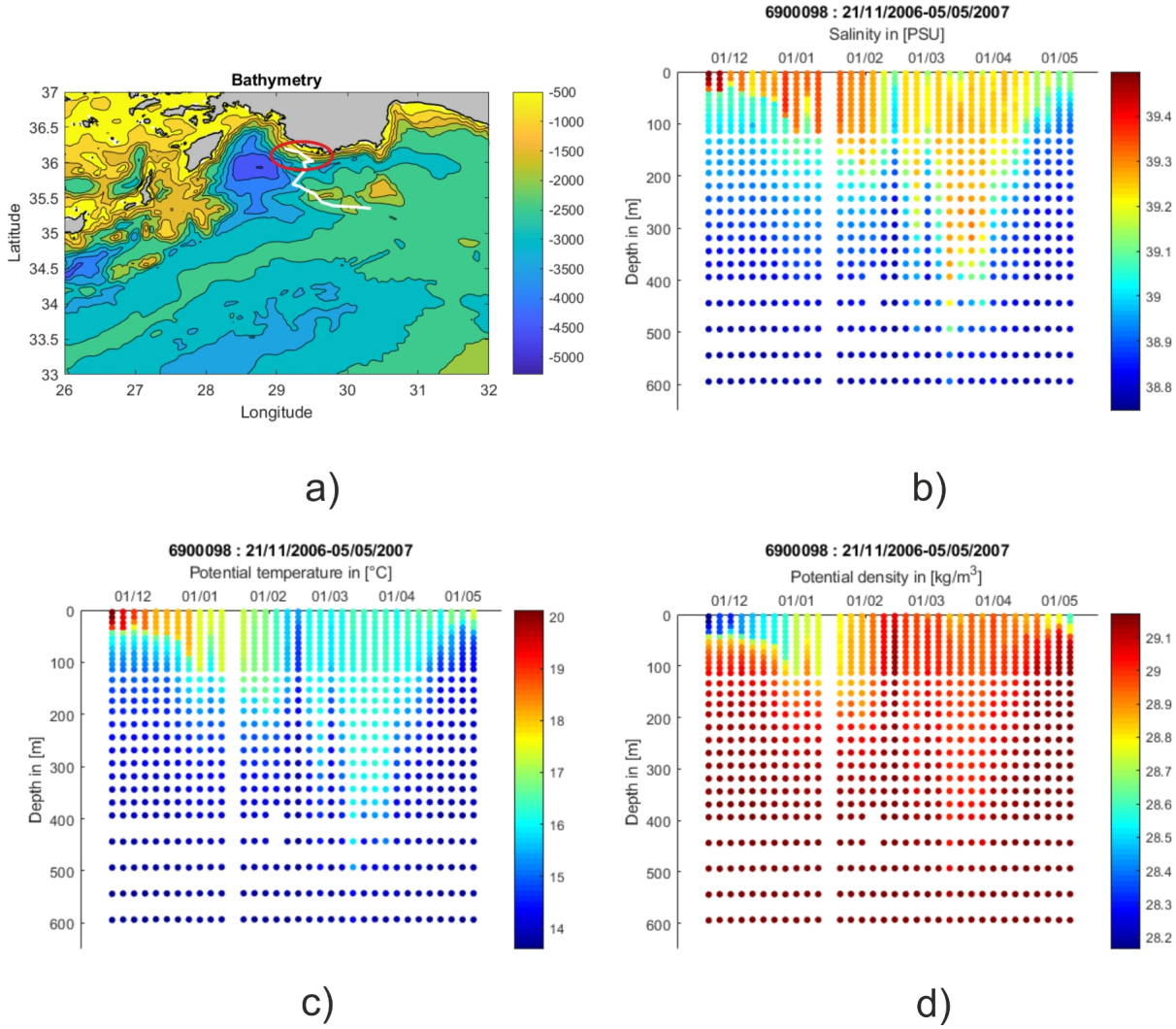

Figure 4.20: a) Bathymetry of the Northwestern Levantine Sea (m) and float trajectory for float WMO 6900096 during JFM 2007. The red circle indicates the position of the float during March when the deep convection event occurred. Hoevmueller plots of **b)** salinity (PSU), **c)** potential temperature (°C), **d)** potential density (kgm^{-3}).

In December and January, very high surface salinity values (S>39.3 psu) can be seen in the upper 50 to 100 m (Figure 4.20b). However, deep mixing and convection is

still prevented by relatively high surface temperatures (T>17 ℃) during this period. Surface temperature has a decreasing trend from about 20 ℃ by the very beginning of December to about 17 ℃ in March when deep convection occurs. By the end of April, the surface temperature gradually increases reaching 17.5 ℃. The observed surface water temperature along the coastline is about 1 ℃ to 3 ℃ warmer than in the open sea (Figures 4.9,4.15,4.20). The MLD deepens gradually from about 50 m within December to about 250 m during February; therefore, the high surface salinity is mixed throughout intermediate layers (Figure 4.20b). By the end of March, when lowest surface temperatures are reached (Figure 4.20c), dense water formation starts to occur. Surface potential density reaches values between 29 and 29.1 kgm^{-3} during this period. The examination of single profiles shows that the mixing event takes place down to about 550 m.

The Hoevmueller plot of the Turner angle (Figure 4.21) reveals statically unstable conditions (|Tu|>90 °; dark blue and dark red points) and therefore a continuous deepening of the MLD in January and February 2007.

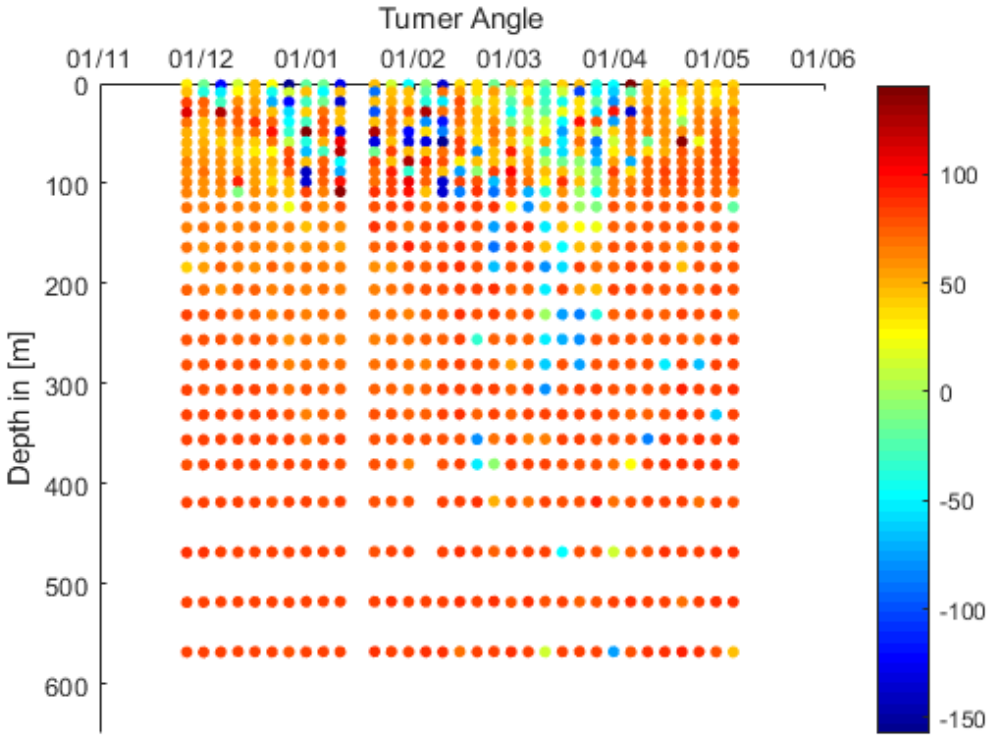

Figure 4.21: The Turner angle (°) of float WMO 6900098 shows the contribution of salinity and temperature gradients to the density gradient.

The main contributors to the stratification in December are both temperature and salinity (-45 °<Tu<45 °), while in April the main contributor is the salinity (45

°<Tu<90 °; yellow and light orange points). The Turner angle indicates the deep LIW formation event down to 550 m in March, which is also characterized by a stronger contribution of temperature gradients (-45 °<Tu<-90 °; blue points).

The T/S plot for March 2007 reveals the formation of typical LIW, i.e., potential temperature above 15 ℃ and salinities higher than 39 psu (Figure 4.22). The potential density lines of 29-29.06 kgm^{-3} represent the potential density range of typical LIW ([9], Figure 4.22).

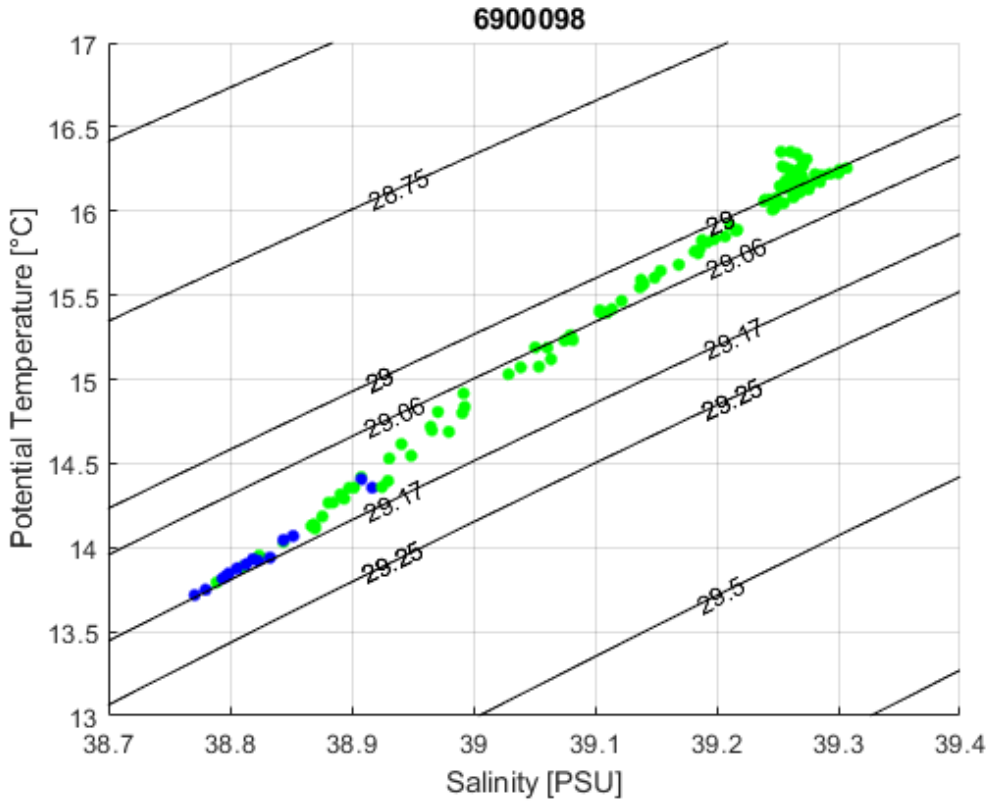

Figure 4.22: T/S plot for float WMO 6900098 for March 2007. Green dots represent depths from 100 to 500 m while blue dots represent depths from 500 to 600 m. The additional density line with a potential density value of 29.17 kgm^{-3} shows the upper deep-water boundary density while the potential density lines of 29-29.06 kgm^{-3} represent the potential density range of typical LIW [9].

The evolution of monthly mean SST from December 2007 to March 2007 is shown in Figure 4.23a-d. The deep convection event that was detected by the Argo float by the end of March 2007, coincides with the strongest depression of SSH and lowest surface temperatures along the coastline during winter 2007 (Figure 4.23e,f).

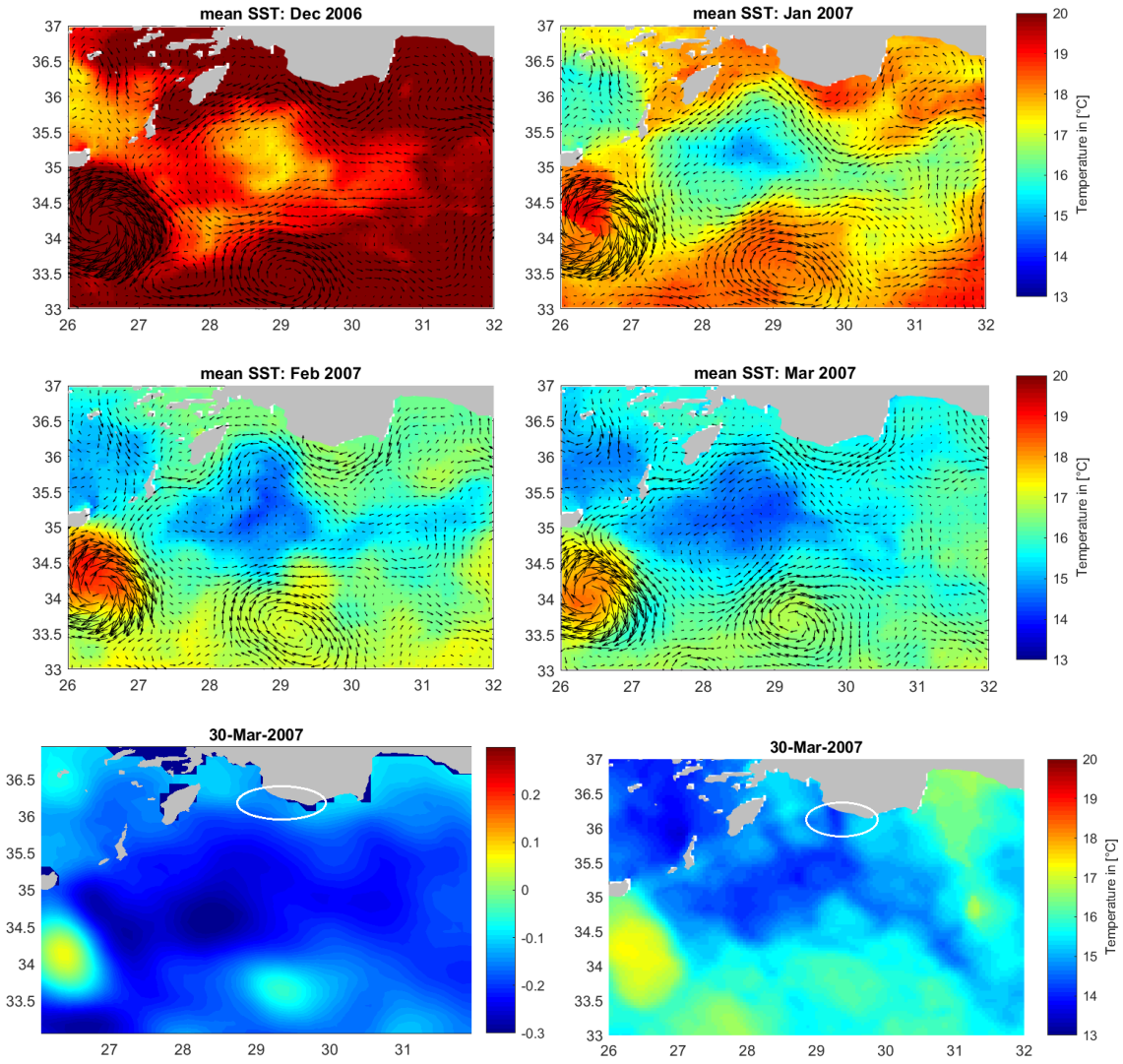

Figure 4.23: Upper and central panel: Monthly mean of satellite SST (°C) from December 2006 to March 2007. Lower panel: SSH (m) and SST (°C) on 30 March 2007, exhibiting strongest depression of SSH and lowest SST within this area during the whole winter period, coinciding with the deep dense water formation event. The white circle indicates the float position during March 2007.

4.2.2.3 Climatology of winter mean MLD

The climatology of the winter (JFM) mean MLD from 2000 to 2018 for the Levantine Sea is shown in Figure 4.24. Within the cyclonic RG, the mean winter MLD is quite shallow (around 70 m). Deeper mean winter MLDs are found within anticyclonic eddies (IE, MME, CE, ShE; see Figure 1.4b for position of eddies) and along the coastlines, indicating dense water formation along boundary currents.

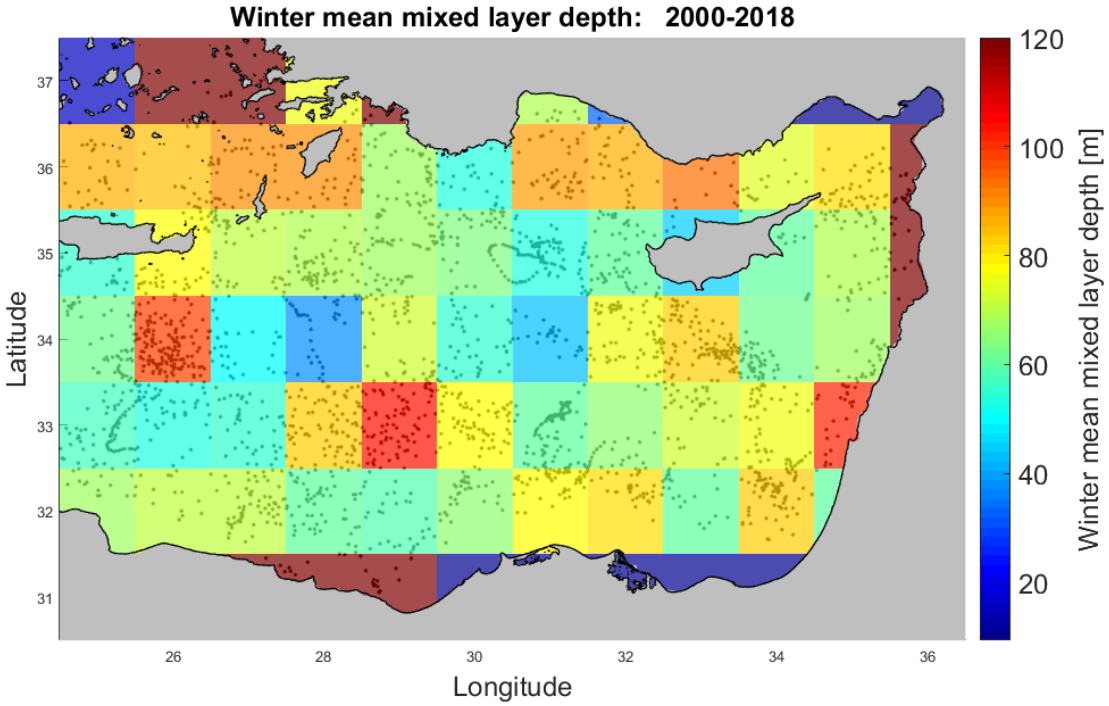

Figure 4.24: Climatology of the winter (JFM) mean MLD from 2000 to 2018 for the Levantine Sea.

4.2.2.4 'LIW Tracking' within the Levantine Sea

Different regions form different intermediate and deeper waters, due to their surface properties [9]. Therefore, T/S diagrams of Argo float data from 2000 to 2017 for diverse areas within the Levantine Sea were plotted, especially for the LIW-core depth (200-500 m) during winter months (JFM).
Figure 4.25 shows the T/S plot for the entire area of the Levantine Sea. The different colors display different depth intervals (yellow from 0 to 100 m, red from 100 to 200 m, green from 200-500 m and blue from 500 to 2000 m). Surface waters exhibit the highest temperature and the highest surface salinity values (the highest surface salinity equals 39.98 psu).
Figure 4.26 shows the characteristics of the LIW (200 to 500 m) for the entire area of the Levantine Sea (the so-called 'scorpion tail image' [29]). The LIW-core (depicted within the red circle), has a potential density of 28.85 kgm^{-3}, a potential temperature of 16.2 ℃and a salinity of 39.1 psu. The subsurface salinity maximum of 39.42 psu is depicted within the black circle.
The LIW characteristics for the entire area of the Levantine Sea during the winter (JFM; Figure 4.27) are characterized by lower temperature values compared to Figure 4.26, while the highest subsurface salinity values are still present.
The T/S plot for the Northwestern Levantine Sea (Figure 4.28) during the winter is characterized by lower temperature and lower salinity values compared to Figure 4.27.
The T/S plot for the center of RG (Figure 4.29) during the winter is characterized by even lower temperature and lower salinity values. Most values lay between the density lines of 29 and 29.17 kgm^{-3} which represents the upper deep boundary layer ([8]; about 1000 m) and therefore indicates deeper and deep dense water formation within the center of RG. Deeper Levantine waters are colder but fresher than the overlaying layers.
The T/S plot for the Northern Levantine coastline during the winter (Figure 4.30,4.31) reveals the formation of typical LIW: Most potential density values lay between 29 and 29.5 kgm^{-3}.
The T/S plot for the Eastern Levantine coastline during the winter (Figure 4.32) shows LIW formation and highest subsurface salinity values, including the subsurface maximum of 39.42 psu.
The T/S plot for the Southern Levantine coastline during the winter (Figure 4.33) exhibits lowest salinity values (<39.2 psu). This is due to the cyclonic rotation of the entering Atlantic Water (AW) within the Levantine Sea (see Figure 1.4b); the longer the distance covered, the more haline (due to evaporation at the air-sea interface) are the sinking water masses.

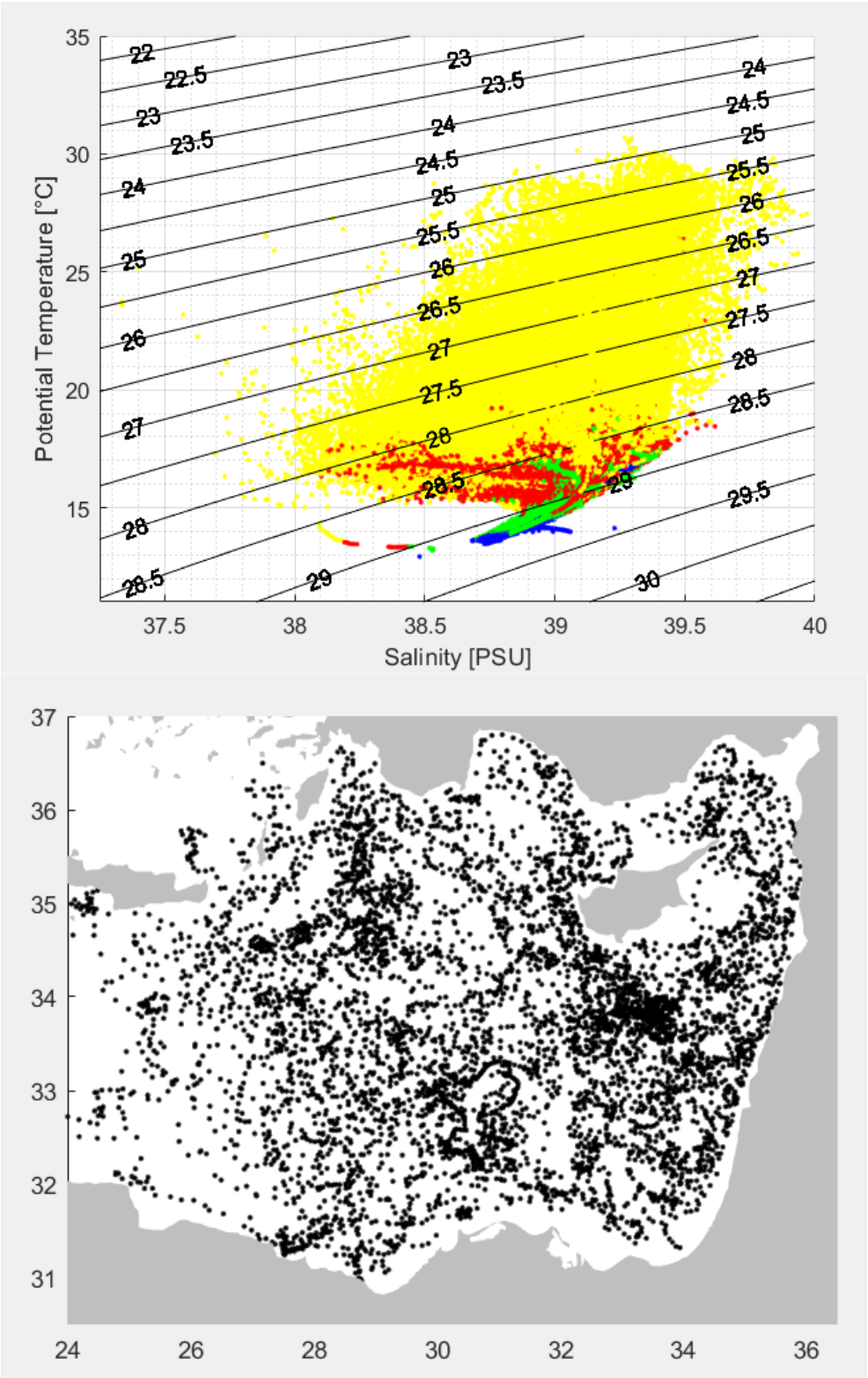

Figure 4.25: Upper panel: T-S plot for the Levantine Sea from 2000 to 2017. Lower panel: Float profiles.

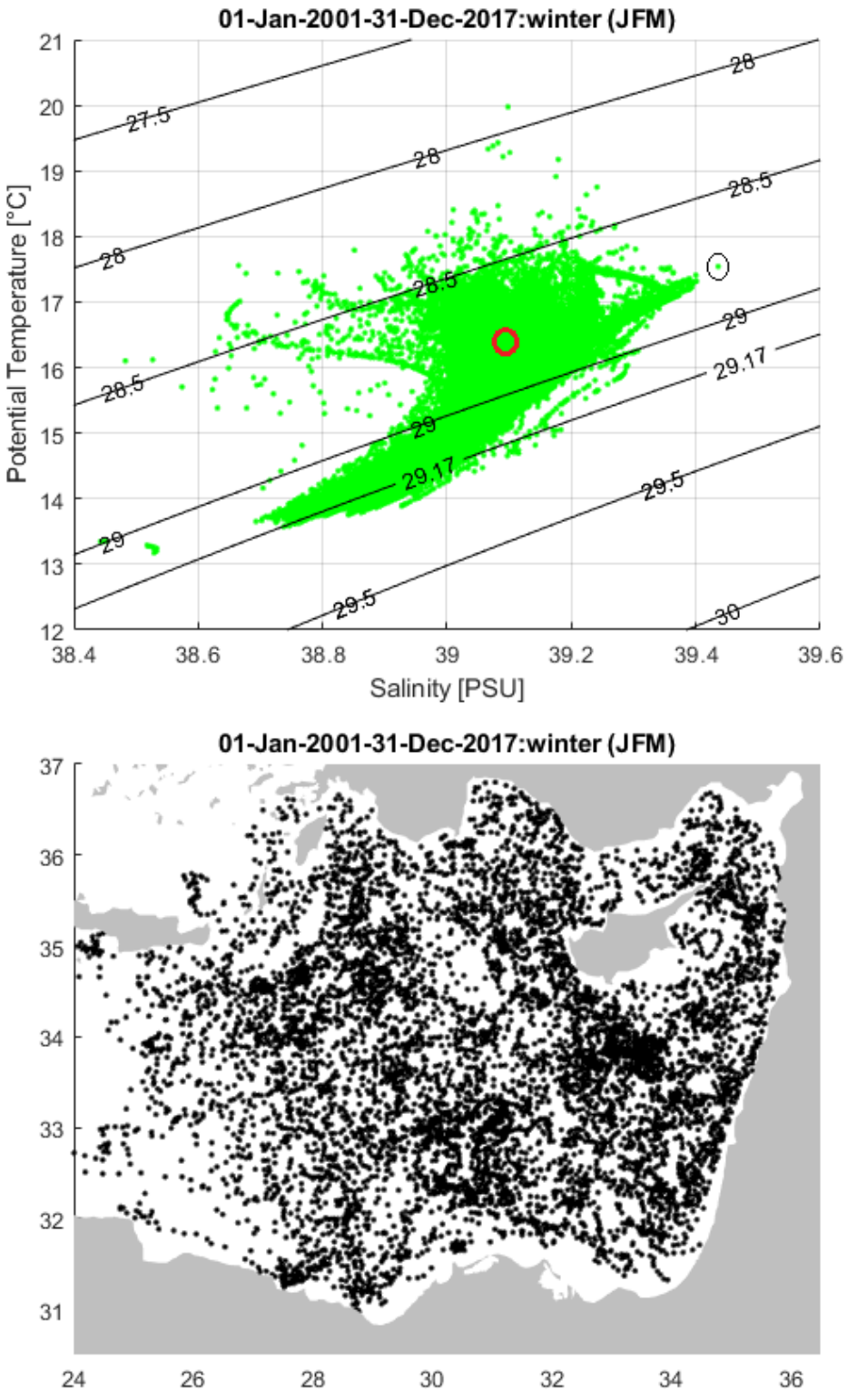

Figure 4.26: Upper panel: T-S plot for intermediate layers (200-500 m) within the Levantine Sea for all months from 2000 to 2017. The red circle indicates the LIW-core and the black circle highlights the largest subsurface salinity value. Lower panel: Float profiles.

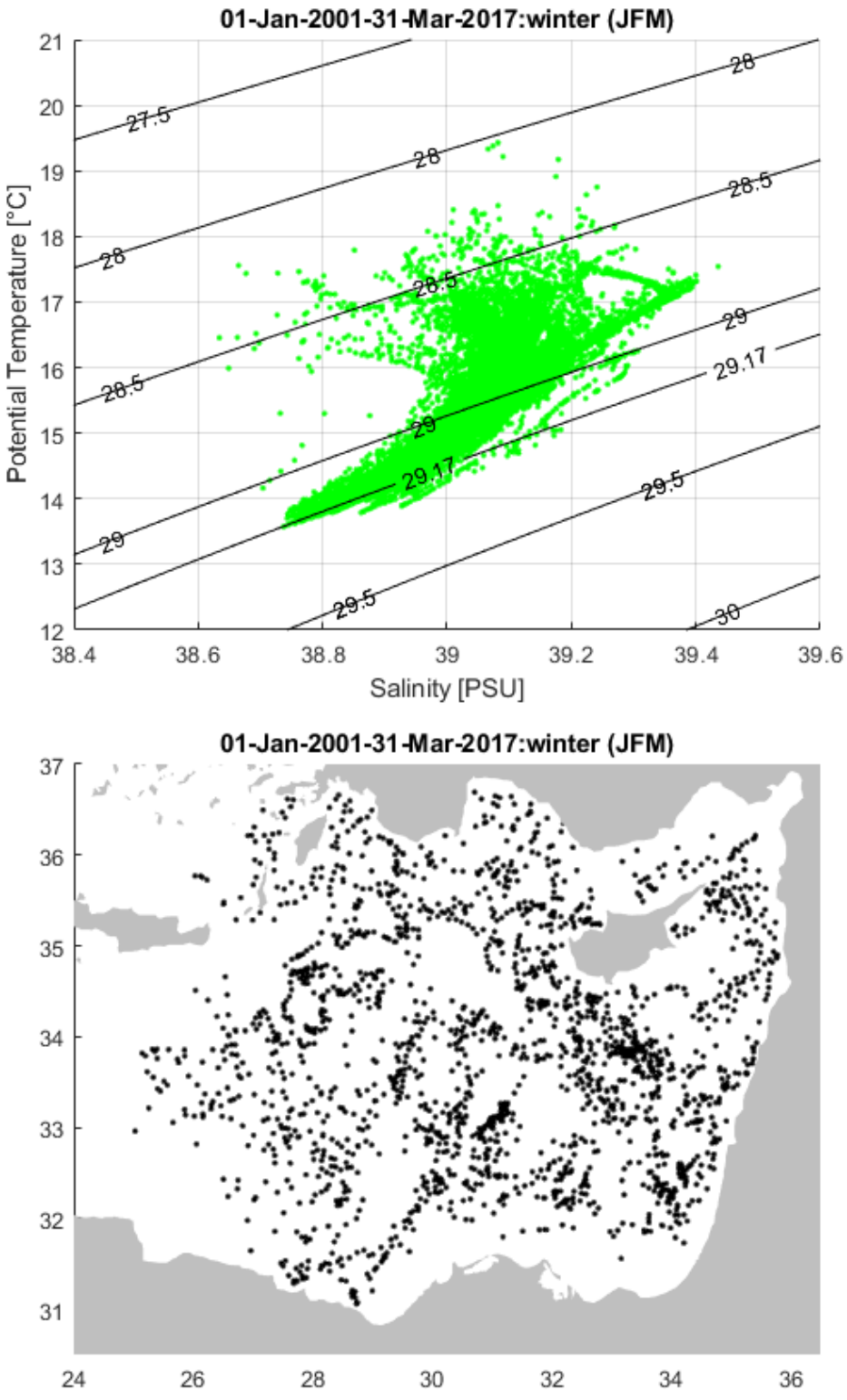

Figure 4.27: Upper panel: T-S plot for intermediate layers (200-500 m) for winter within the Levantine Sea from 2000 to 2017. Lower panel: Float profiles.

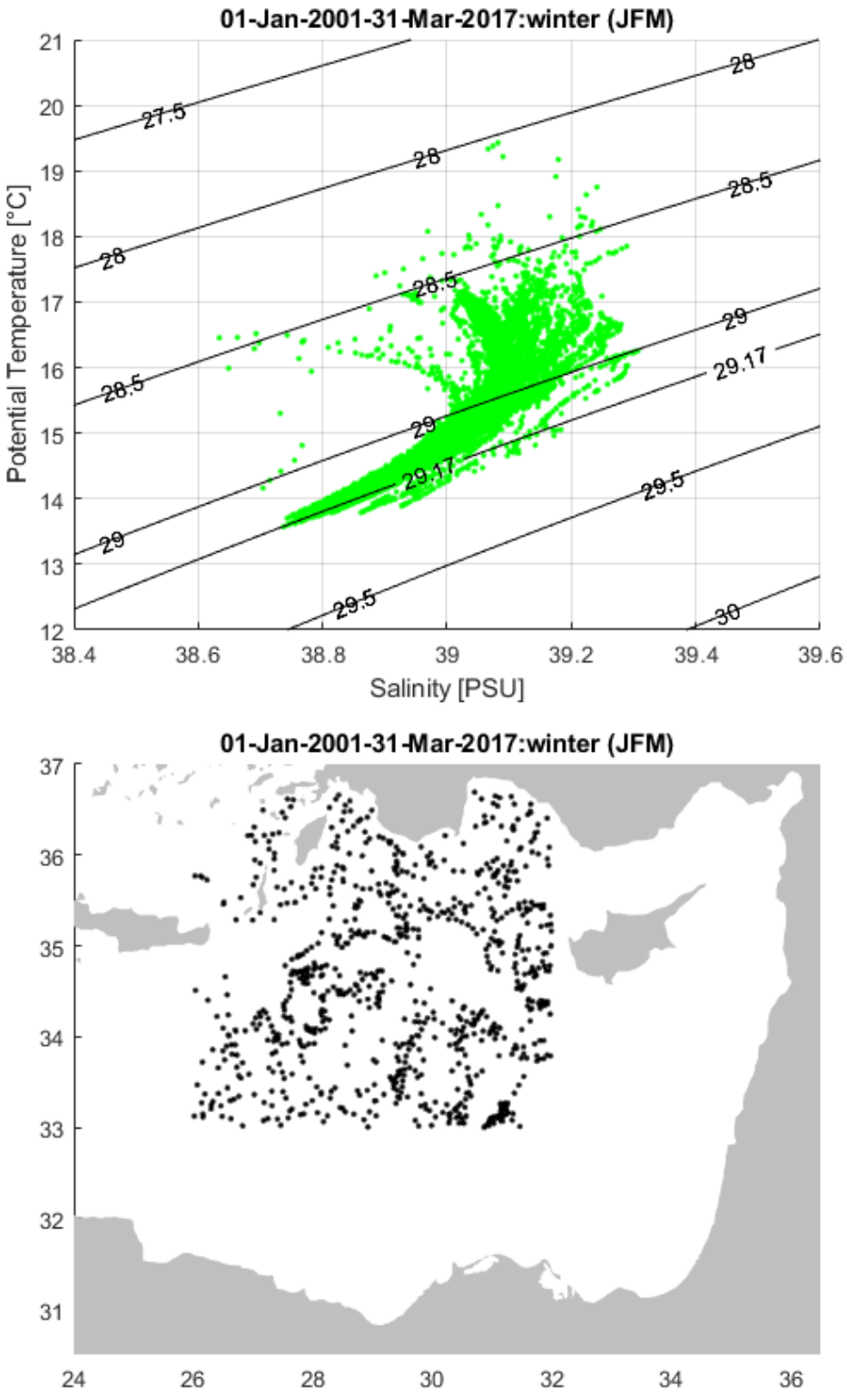

Figure 4.28: Upper panel: T-S plot for intermediate layers (200-500 m) for winter within the Northwestern Levantine Sea from 2000 to 2017. Lower panel: Float profiles.

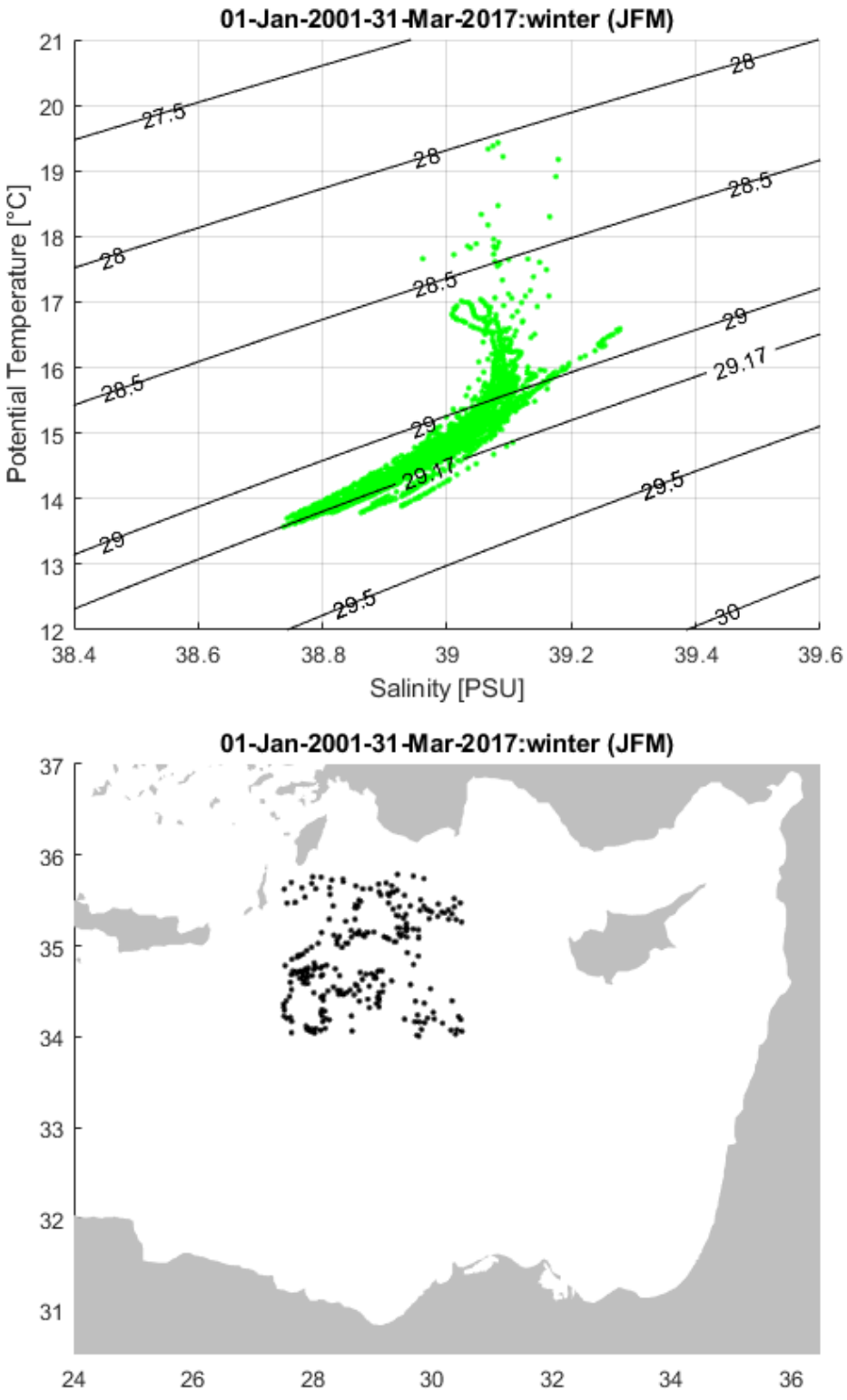

Figure 4.29: Upper panel: T-S plot for intermediate layers (200-500 m) for winter within the center of Rhodes Gyre from 2000 to 2017. Lower panel: Float profiles.

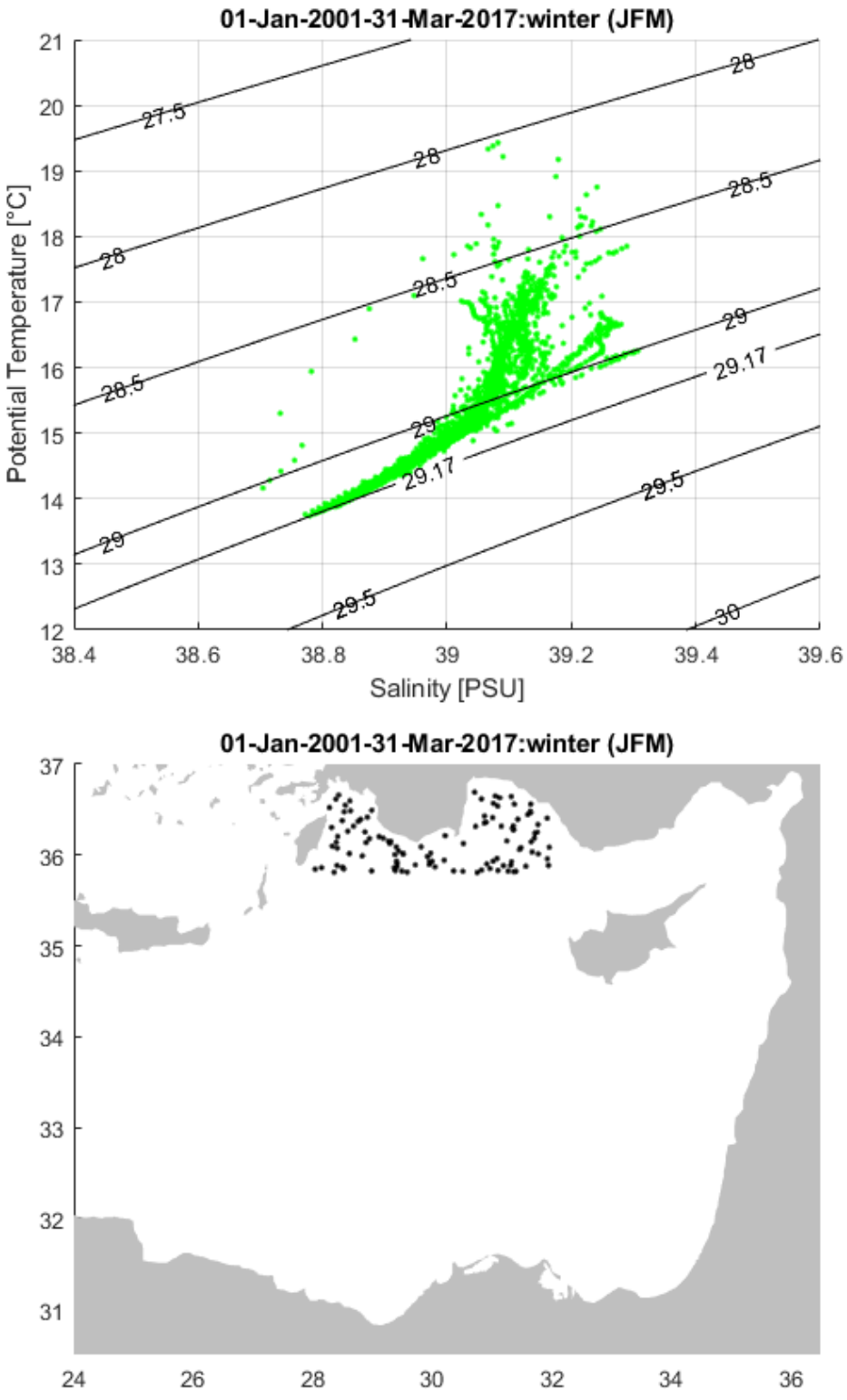

Figure 4.30: Upper panel: T-S plot for intermediate layers (200-500 m) for winter along the Northwestern coastline from 2000 to 2017. Lower panel: Float profiles.

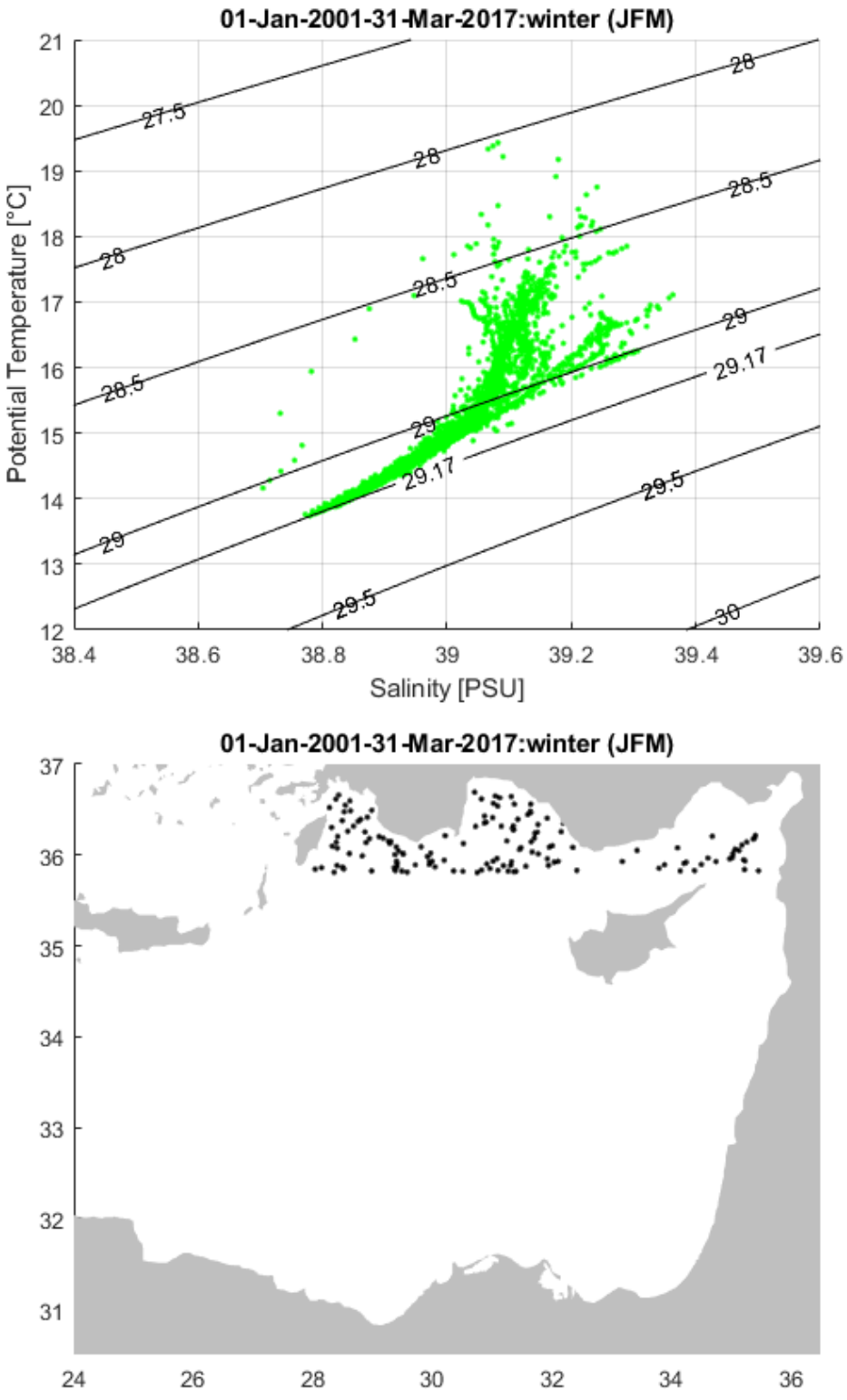

Figure 4.31: Upper panel: T-S plot for intermediate layers (200-500 m) for winter along the Northern coastline from 2000 to 2017. Lower panel: Float profiles.

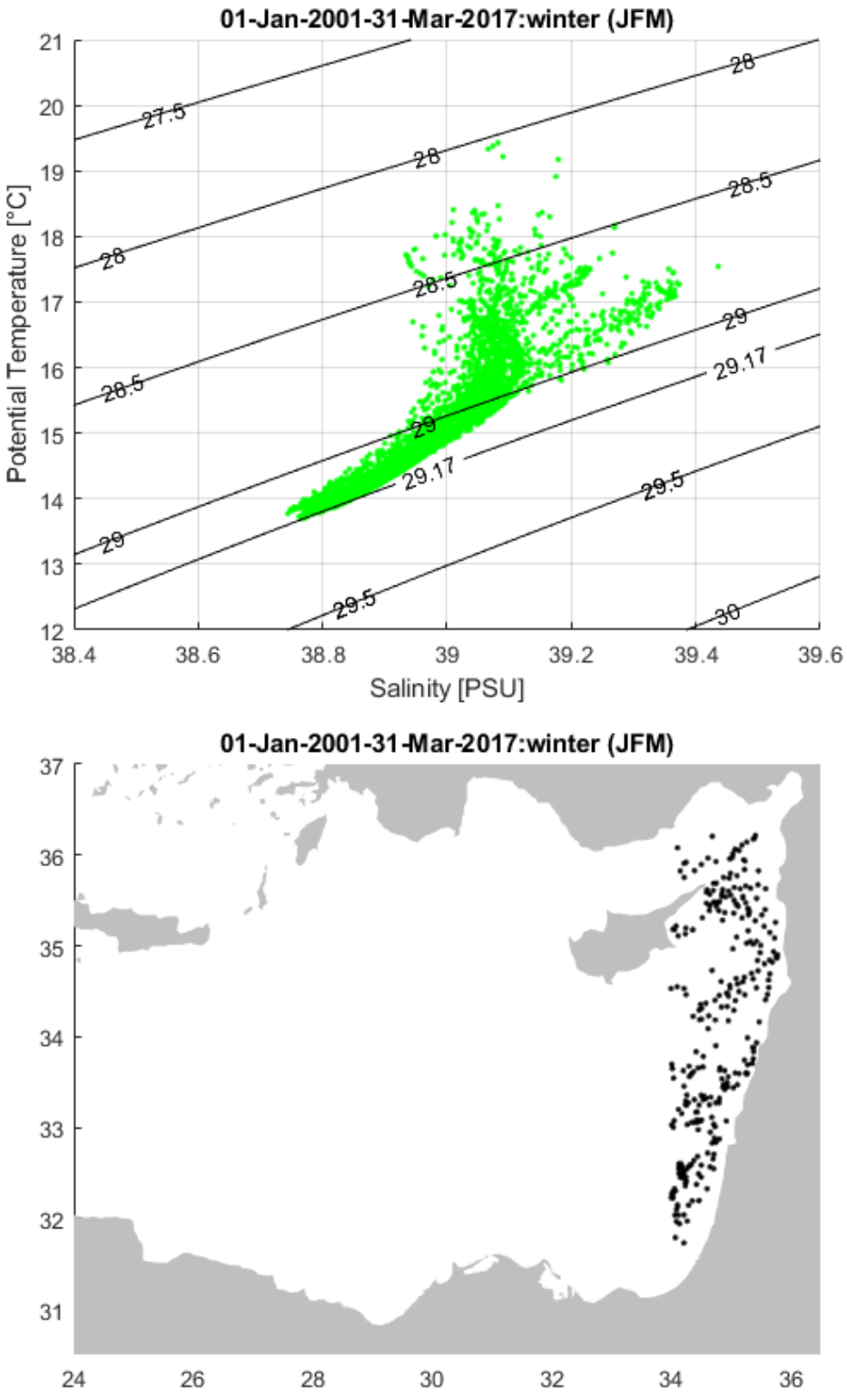

Figure 4.32: Upper panel: T-S plot for intermediate layers (200-500 m) for winter along the Eastern coastline from 2000 to 2017. Lower panel: Float profiles.

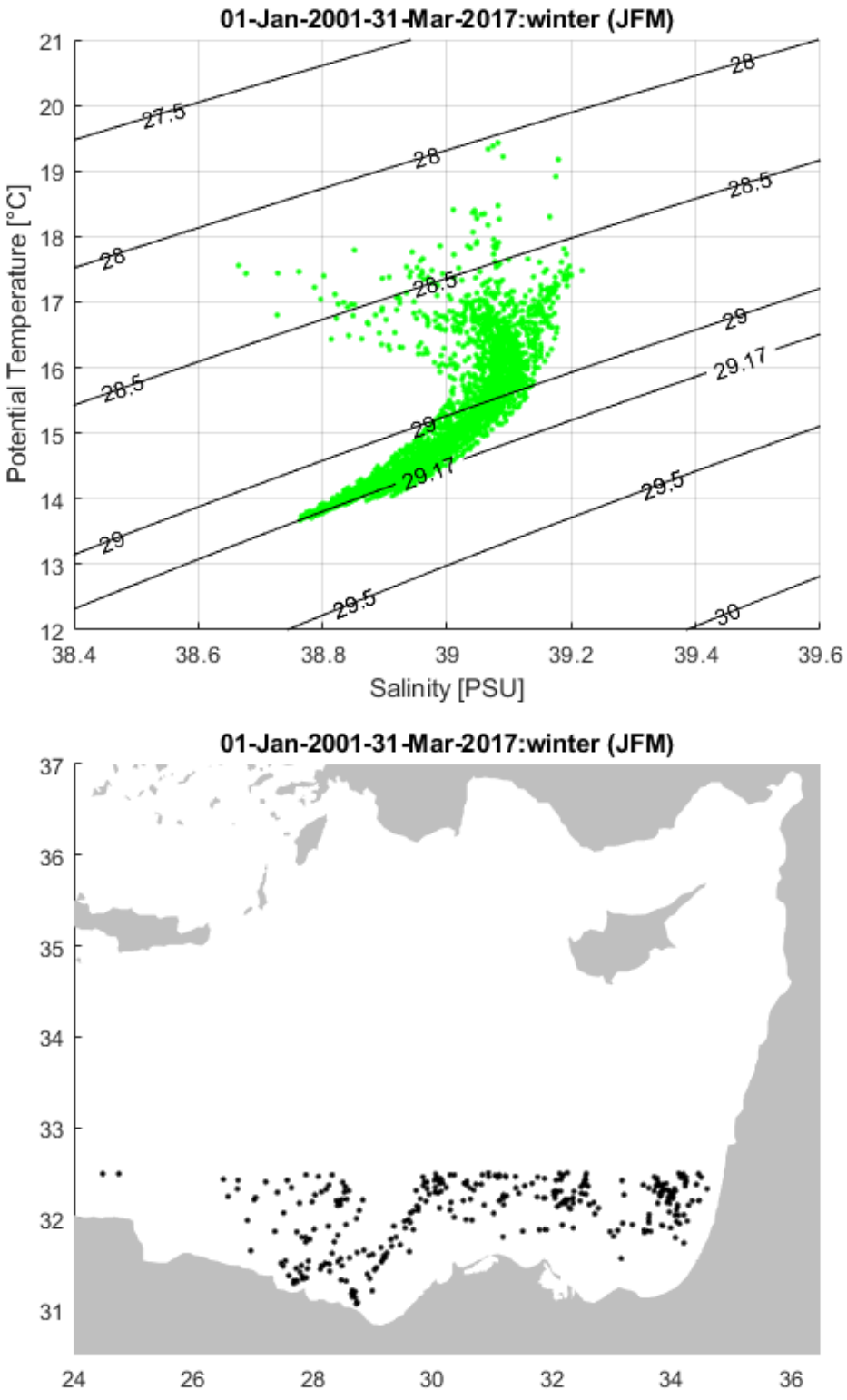

Figure 4.33: Upper panel: T-S plot for intermediate layers (200-500 m) for winter along the Southern coastline from 2000 to 2017. Lower panel: Float profiles.

Chapter 5

Discussion and Conclusions

5.1 Statistics of the Levantine Sea

5.1.1 Float speed and residence time

The float speed and residence time for different parking depths give a better understanding of the circulation of intermediate and deeper water masses and are also important for a better understanding of ecological issues: Dense water that sinks can be polluted and travels for decades or centuries before it surfaces at another place within the Mediterranean Sea (so our children and our great grandchildren will have to face it!), e.g. 95 % of microplastics in the Northern Adriatic are imported by intermediate waters.
To estimate the transport of microplastics it is crucial to know the speed and the residence time of different water masses. Therefore the mean float speed and the mean float residence time have been calculated and plotted for two different parking depths (PD=350 m and PD=1000 m).
The mean speed of intermediate water (PD=350 m) is 3.9 cm/s and the mean speed of deeper water (PD=1000 m) is 2.9 cm/s (Figure 4.1,4.2,4.3). A rough estimate of 'travelling time' of intermediate water is given in Section 4.1.1.

From the $1° \times 1°$ plot of mean speed general features like the Mid Mediterranean jet (MMJ) can be seen. The $1° \times 1°$ plot of mean residence time reveals that Levantine Deep Water (LDW) is trapped within the the two main circulation subsystems of the Levantine Sea, i.e. Rhodes Gyre (RG) and Cyprus Eddy, while the LIW is mainly influenced by the upper circulation (Figure 4.3).

Float speed and residence time are also useful for further float deployments: To obtain a good float coverage of the Levantine Sea, the float deployments should take place in areas of low mean residence times, though not in areas of high numbers of lost floats, e.g. a float deployed at the beginning of the Asia Minor Current (latitude: 35 °-36 °,

longitude: 34 °-35 °) could travel all the Levantine Sea, taking advantage of its overall cyclonic circulation.

5.1.2 Mixed layer depth and ocean heat content

Diapycnal mixing and convection transfer and distribute heat to intermediate, deeper and abyssal layers [30]. The two phenomena act on different time scales [31, 32]. Coexisting stable stratification, deep mixing, intense meridional overturning circulation and mesoscale eddies affect the heat content distribution within the Eastern Mediterranean surface, intermediate and abyssal waters [33].

In fact, the $1° \times 1°$ climatologies of the mean OHC for the area of the Levantine Sea from 2000 to 2017 (Figure 4.5) reveals that the mean OHC is lowest in areas of net upwelling, i.e. in cyclonic structures such as RG and largest in areas of net downwelling, i.e. in anticylconic structures such as Cyprus Eddy. Also the influence of the anticyclonic EE, MME and IE (see Figure 1.4b for position of eddies) on deeper layers (<500 m) can be seen.

The $1° \times 1°$ climatology of the winter mean MLD for the area of the Levantine Sea from 2000 to 2017 indicates deepest MLDs within eddies and gyres (RG, IE, MME, CE, LTE; see Figure 1.4b for position of eddies) and along the Levantine coastline. Deep dense water formation events are not indicated by the MLD climatology, due to the process of recapping (described in Section 3.1.5).

5.2 Levantine intermediate and levantine deep water formation

The present study is focused on the LIW and LDW formation events in the NWLS (Figure 5.1a) as detected by Argo float data from 2001 to 2017. The new and most interesting result is that the typical LIW (potential temperature>15 ℃ and salinity>39 psu) formation mainly occurred along the Northern coastline (Figures 4.22,4.30), while 'lower range' LIW (potential temperature about 15 ℃ and salinity about 39 psu) and LDW (13.7 ℃<potential temperature<14.5 ℃, 38.8 psu<salinity<38.9 psu) formation took place within mesoscale eddies located within the center of RG (Figures 5.1a, 4.14a,4.29, Table 4.1).

The schematic summary of the results for the winter seasons from 2001 to 2017 is evident in Figure 5.1b. Blue and brown arrows describe the convection and net sinking areas of the Mediterranean Sea as derived from theoretical models by [5, 22]. Red and orange arrows are derived from the results of the present work. Red solid and dashed lines represent the formation of intermediate (200-500 m) and deeper waters (500-600 m) along the Northern coastline. Orange arrows represent the formation of intermediate (200-500 m) and deep waters (about 1000 m) within the RG, respectively. The examination of individual profiles showed dense water formation events reaching down to 550 m depth along the coastline and down to 1000 m depth within the center of RG (Figure 5.1b).

The specific event of LIW formation, captured by the Argo float data in March 2007 along the coastline, reached a depth of about 550 m. The T/S plot (Figure 4.22) showed typical LIW formation during this event and the observed surface water temperature along the coastline was about 1 ℃ to 3 ℃ warmer than in the open sea (Figures 4.9,4.15,4.20), in agreement with the results of [34, 35].
In January-February 2006, the Argo float data detected LDW formation in the core of a cyclonic mesoscale structure located in the center of RG. This structure (diameter of about 60 km) shows the typical horizontal scale of convective chimneys. The T/S plot in Figure 4.14a reveals the LDW characteristics of the convection event. All potential temperatures and salinity values lay on the line of constant potential density of 29.17 kgm^{-3}, revealing the sinking of the formed water masses to at least 1000 m as previously observed [9, 16, 17].

The intensity of the mixing and convection events depends mainly on the surface buoyancy flux B, which in turn depends on its thermal (B_T) and haline (B_S) components. The calculation and plot of the surface buoyancy flux and its components revealed that the haline component dominates over the thermal component (Figure 4.7, lower panel), i.e., intense evaporation (B_S<0) controls the surface buoyancy

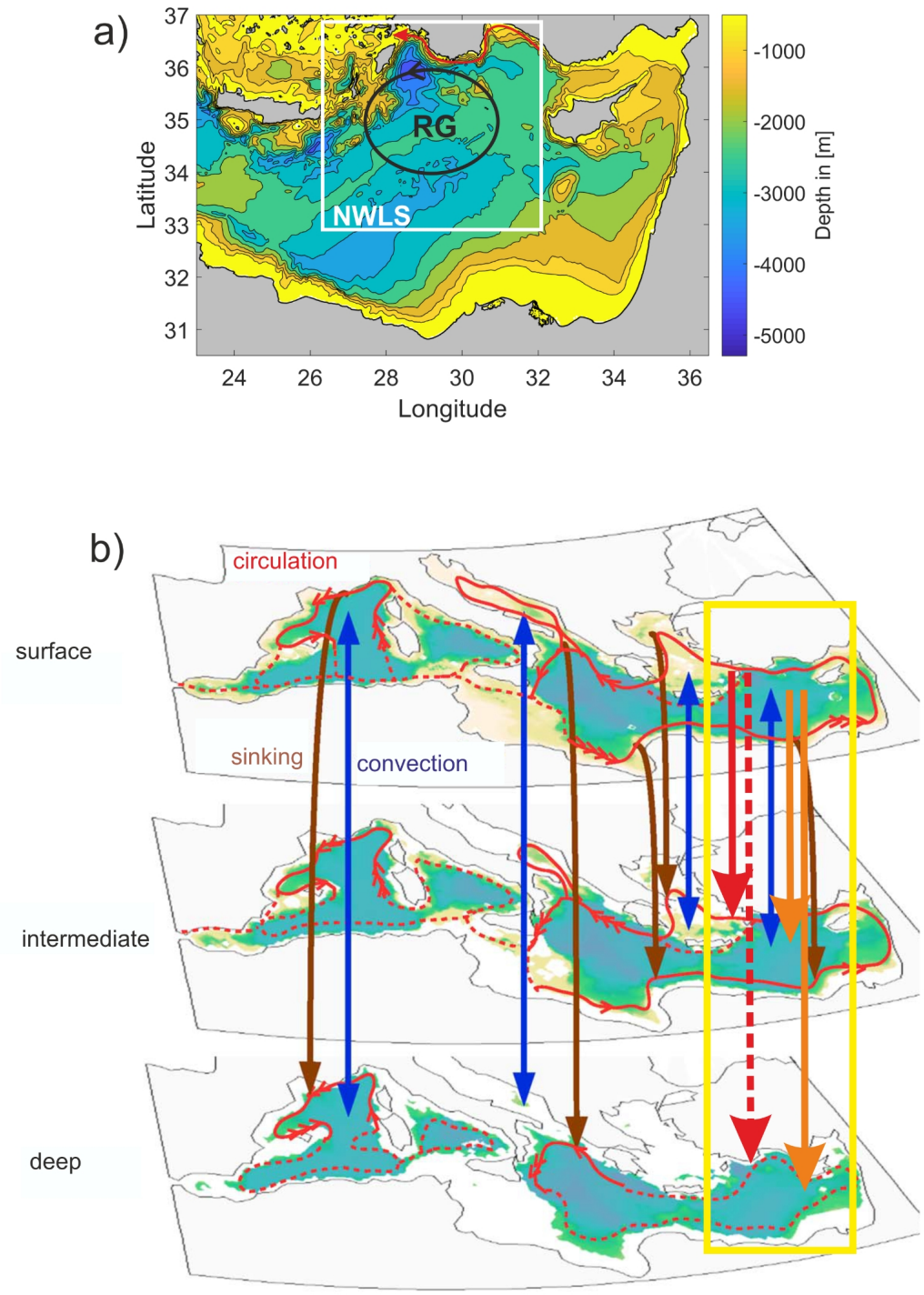

Figure 5.1: a) The white rectangle confines the area of study, the NWLS. Typical LIW formation was found along the Northern coastline (red arrow), while 'lower range' LIW and LDW formation was found within submesoscale eddies within the center of RG (black ellipse). b) This figure, adapted from [5], summarizes the obtained results for winter seasons in the NWLS (yellow rectangle) : Dense water formation along the Northern coastline reached intermediate (200-500 m; red line) and deeper layers (500-600 m; dashed red line), while LDW formation within the center of RG reached intermediate and deep layers (at least 1000 m; orange lines).

loss, especially during the preconditioning phase (e.g., Figure 4.118 for winter 2006). Therefore, the area of the RG is an area of net buoyancy loss, driven by the haline component, as shown by [36].

The influence of salinity and temperature gradients to the density gradients are described in the Hoevmueller diagrams of the Turner angle (Figures 4.10,4.16,4.21). During the preconditioning phase (November, December) and the constant deepening of the MLD in the beginning of January, the influence of the salinity gradient was dominant, while during strong unstable conditions and consequently dense water formation, also the temperature gradient was influential. The Turner angle also approximately indicated the depth of the convection events.

The deep dense water formation events within the area of the RG can be described by the following phases: The whole process is influenced by the cyclonic rotation of the RG leading to the upwelling of cooler waters to the surface. In November and December, the preconditioning phase starts (Figures 4.7,4.8): the heat losses due to cold and dry winds lead to increased surface salinity (Figures 4.9,4.15,4.20) through the evaporation and to a steady deepening of the MLD. Additional, temporarily outbreaks of strong winds during January, February, or March cause strong heat losses (Figures 4.8,4.11), which cause further cooling of surface waters. When lowest surface temperatures are reached (Figures 4.13,4.19,4.23), dense water formation starts to occur. Within hours, the newly formed dense water sinks down rapidly to a depth of equal density where it spreads horizontally, forming an anticyclonic circulation due to the influence of the Coriolis force.

The convection event also implicates a stretching of the water column leading to a change in vorticity, an increased geostrophic velocity, and a depression of the SSH. In fact, all pronounced dense water formation events documented by the Argo floats were indicated by a strong depression of satellite SSH (Figures 4.12,4.18,4.23) and by lowest SSTs (Figures 4.13,4.19,4.23).

The Argo float data revealed that LDW formation took place within the RG during winter months and showed the key role of the boundary currents for the LIW formation. The climatology of the mean MLDs of the Levantine Sea (Figure 4.24) reveals that, despite the deep convection events, little to net mean sinking takes place within the center of RG, while the deeper MLDs along the coastline indicate dense water formation occurring along boundary currents.
Therefore, the drivers, sources, and main contributors of the Mediterranean thermohaline circulation have to be rethought not only within the Levantine, but also within the Mediterranean Sea. Deployments of additional Argo floats to survey boundary

currents and deployment of deep Argo floats within the main Mediterranean convection sites, i.e., the Gulf of Lion, the South Adriatic, and the RG area, will contribute to further understanding of dense water formation processes.

A better understanding of the Mediterranean thermohaline circulation is needed not only for a wider knowledge of the effects of climate change, but also for the impact on ecology. Newly formed intermediate or deep waters can be polluted (with oil, microplastics, nutrients from extensive agriculture, heat due to global warming etc.), e.g., the Northern Levantine coastline, where pronounced dense water formation occurs, has the highest coastline plastic pollution within the Mediterranean Sea [37]. The newly formed water masses with the above-mentioned water properties and pollutants are transported throughout the Mediterranean to finally reach the Atlantic Ocean.
The full impact (in terms of pollution and different water mass characteristics) will only be seen by future generations when these water masses emerge after decades or even centuries at different places within the Mediterranean Sea.

Therefore, it is obvious and evident that scientists and policy makers are obliged to join forces *now* to support and make commitments towards a real sustainable world that is not threatening, but protecting our ecosystems and lives.

Bibliography

[1] N. Pinardi, M. Zavatarelli, M. Adani, G. Coppini, C. Fratianni, P. Oddo, S. Simoncelli, M. Tonani, V. Lyubartsev, S. Dobricic, *et al.*, "Mediterranean sea large-scale low-frequency ocean variability and water mass formation rates from 1987 to 2007: A retrospective analysis," *Progress in Oceanography*, vol. 132, pp. 318–332, 2015.

[2] R. X. Huang, *Ocean circulation: wind-driven and thermohaline processes*. Cambridge University Press, 2010.

[3] M. N. Tsimplis, V. Zervakis, S. A. Josey, E. L. Peneva, M. V. Struglia, E. V. Stanev, A. Theocharis, P. Lionello, P. Malanotte-Rizzoli, V. Artale, *et al.*, "Changes in the oceanography of the mediterranean sea and their link to climate variability," in *Developments in earth and environmental sciences*, vol. 4, pp. 227–282, Elsevier, 2006.

[4] M. Menna, P.-M. Poulain, G. Zodiatis, and I. Gertman, "On the surface circulation of the levantine sub-basin derived from lagrangian drifters and satellite altimetry data," *Deep Sea Research Part I: Oceanographic Research Papers*, vol. 65, pp. 46–58, 2012.

[5] R. Waldman, N. Brüggemann, A. Bosse, M. Spall, S. Somot, and F. Sevault, "Overturning the mediterranean thermohaline circulation," *Geophysical Research Letters*, vol. 45, no. 16, pp. 8407–8415, 2018.

[6] R. H. Stewart, *Introduction to physical oceanography*. Texas A & M University College Station, 2008.

[7] ArgoCommunity, "Argo program–the global ocean observing system.," 2019.

[8] W. Roether, B. Klein, B. B. Manca, A. Theocharis, and S. Kioroglou, "Transient eastern mediterranean deep waters in response to the massive dense-water output of the aegean sea in the 1990s," *Progress in Oceanography*, vol. 74, no. 4, pp. 540–571, 2007.

[9] P. Malanotte-Rizzoli, B. Manca, S. Marullo, M. Ribera d'Alcala', W. Roether, A. Theocharis, A. Bergamasco, G. Budillon, E. Sansone, G. Civitarese, *et al.*, "The levantine intermediate water experiment (liwex) group: Levantine basinŮa laboratory for multiple water mass formation processes," *Journal of Geophysical Research: Oceans*, vol. 108, no. C9, 2003.

[10] A. Bergamasco and P. Malanotte-Rizzoli, "The circulation of the mediterranean sea: a historical review of experimental investigations," *Advances in Oceanography and Limnology.*, vol. 1, no. 1, pp. 11–28, 2010.

[11] M. Gačić, G. Civitarese, G. Eusebi Borzelli, V. Kovačević, P.-M. Poulain, A. Theocharis, M. Menna, A. Catucci, and N. Zarokanellos, "On the relationship between the decadal oscillations of the northern ionian sea and the salinity distributions in the eastern mediterranean," *Journal of Geophysical Research: Oceans*, vol. 116, no. C12, 2011.

[12] M. Gačić, K. Schroeder, G. Civitarese, A. Vetrano, and G. Eusebi Borzelli, "On the relationship among the adriatic–ionian bimodal oscillating system (bios), the eastern mediterranean salinity variations and the western mediterranean thermohaline cell," *Ocean Science Discussions*, vol. 9, no. 4, pp. 2561–2580, 2012.

[13] M. Menna, N. R. Suarez, G. Civitarese, M. Gačić, A. Rubino, and P.-M. Poulain, "Decadal variations of circulation in the central mediterranean and its interactions with mesoscale gyres," *Deep Sea Research Part II: Topical Studies in Oceanography*, 2019.

[14] A. Theocharis, G. Krokos, D. Velaoras, and G. Korres, "An internal mechanism driving the alternation of the eastern mediterranean dense/deep water sources," *The Mediterranean Sea: Temporal Variability and Spatial Patterns*, vol. 10, pp. 113–137, 2014.

[15] P. Lionello, P. Malanotte-Rizzoli, R. Boscolo, P. Alpert, V. Artale, L. Li, J. Luterbacher, W. May, R. Trigo, M. Tsimplis, *et al.*, "The mediterranean climate: an overview of the main characteristics and issues," 2006.

[16] H. Sur, E. Özsoy, and Ü. Ünlüata, "Simultaneous deep and intermediate depth convection in the northern levantine sea, winter 1992," *Oceanologica Acta*, vol. 16, no. 1, pp. 33–43, 1993.

[17] I. Gertmann, I. Ovchinnikov, and Y. I. Popv, "Deep convection in the eastern basin of the mediterranean sea," *Oceanology*, vol. 34, no. 1, pp. 19–25, 1994.

[18] M. A. Spall and R. S. Pickart, "Where does dense water sink? a subpolar gyre example," *Journal of Physical Oceanography*, vol. 31, no. 3, pp. 810–826, 2001.

[19] M. A. Spall, "Boundary currents and watermass transformation in marginal seas," *Journal of physical oceanography*, vol. 34, no. 5, pp. 1197–1213, 2004.

[20] M. A. Spall, "Buoyancy-forced downwelling in boundary currents," *Journal of Physical Oceanography*, vol. 38, no. 12, pp. 2704–2721, 2008.

[21] M. A. Spall, "Dynamics of downwelling in an eddy-resolving convective basin," *Journal of Physical Oceanography*, vol. 40, no. 10, pp. 2341–2347, 2010.

[22] N. Pinardi, P. Cessi, F. Borile, and C. L. Wolfe, "The mediterranean sea overturning circulation," *Journal of Physical Oceanography*, vol. 49, no. 7, pp. 1699–1721, 2019.

[23] S. A. Thorpe, *The turbulent ocean*. Cambridge University Press, 2005.

[24] G. K. Vallis, *Essentials of Atmospheric and Oceanic Dynamics*. Cambridge University Press, 2019.

[25] B. Cushman-Roisin and J.-M. Beckers, *Introduction to geophysical fluid dynamics: physical and numerical aspects*, vol. 101. Academic press, 2011.

[26] S. Martin, *An introduction to ocean remote sensing*. Cambridge University Press, 2014.

[27] P.-M. Poulain, R. Barbanti, J. Font, A. Cruzado, C. Millot, I. Gertman, A. Griffa, A. Molcard, V. Rupolo, S. Le Bras, *et al.*, "Medargo: a drifting profiler program in the mediterranean sea," 2007.

[28] J. Holte, L. D. Talley, J. Gilson, and D. Roemmich, "An argo mixed layer climatology and database," *Geophysical Research Letters*, vol. 44, no. 11, pp. 5618–5626, 2017.

[29] C. Millot, "Levantine intermediate water characteristics: an astounding general misunderstanding!," *Scientia Marina*, vol. 77, no. 2, pp. 217–232, 2013.

[30] S. Levitus, J. I. Antonov, T. P. Boyer, and C. Stephens, "Warming of the world ocean," *Science*, vol. 287, no. 5461, pp. 2225–2229, 2000.

[31] J. Marotzke and J. R. Scott, "Convective mixing and the thermohaline circulation," *Journal of Physical Oceanography*, vol. 29, no. 11, pp. 2962–2970, 1999.

[32] J. Marshall and F. Schott, "Open-ocean convection: Observations, theory, and models," *Reviews of Geophysics*, vol. 37, no. 1, pp. 1–64, 1999.

[33] V. Artale, F. Falcini, S. Marullo, M. Bensi, F. Kokoszka, D. Iudicone, and A. Rubino, "Linking mixing processes and climate variability to the heat content distribution of the eastern mediterranean abyss," *Scientific reports*, vol. 8, no. 1, p. 11317, 2018.

[34] Y. Feliks, "Downwelling along the northeastern coasts of the eastern mediterranean," *Journal of physical oceanography*, vol. 21, no. 4, pp. 511–526, 1991.

[35] Y. Feliks and M. Ghil, "Downwelling-front instability and eddy formation in the eastern mediterranean," *Journal of physical oceanography*, vol. 23, no. 1, pp. 61–78, 1993.

[36] J. Karstensen and K. Lorbacher, "A practical indicator for surface ocean heat and freshwater buoyancy fluxes and its application to the ncep reanalysis data," *Tellus A: Dynamic Meteorology and Oceanography*, vol. 63, no. 2, pp. 338–347, 2011.

[37] WWF, "Mediterranean marine initiative report. stop the flood of plastic: How mediterranean countries can save their sea," 2019.